INTERNATIONAL JOURNAL FOR NUMERICAL METHODS IN FLUIDS
Int. J. Numer. Meth. Fluids 2015; **77**:159–182
Published online 25 November 2014 in Wiley Online Library (wileyonlinelibrary.com). DOI: 10.1002/fld.3983

A two-dimensional numerical scheme of dry/wet fronts for the Saint-Venant system of shallow water equations

Zsolt Horváth[1,2,*,†], Jürgen Waser[2], Rui A. P. Perdigão[1], Artem Konev[2] and Günter Blöschl[1,3]

[1]*Institute of Hydraulic Engineering and Water Resources Management, Vienna University of Technology, Karlsplatz 13/222, 1040 Vienna, Austria*
[2]*VRVis Zentrum für Virtual Reality und Visualisierung Forschungs-GmbH, Donau-City-Strasse 1, 1220 Vienna, Austria*
[3]*Centre for Water Resource Systems, Vienna University of Technology, Karlsplatz 13, 1040 Vienna, Austria*

SUMMARY

We propose a new two-dimensional numerical scheme to solve the Saint-Venant system of shallow water equations in the presence of partially flooded cells. Our method is well balanced, positivity preserving, and handles dry states. The latter is ensured by using the draining time step technique in the time integration process, which guarantees non-negative water depths. Unlike previous schemes, our technique does not generate high velocities at the dry/wet boundaries, which are responsible for small time step sizes and slow simulation runs. We prove that the new scheme preserves 'lake at rest' steady states and guarantees the positivity of the computed fluid depth in the partially flooded cells. We test the new scheme, along with another recent scheme from the literature, against the analytical solution for a parabolic basin and show the improved simulation performance of the new scheme for two real-world scenarios. Copyright © 2014 John Wiley & Sons, Ltd.

Received 15 July 2014; Revised 13 October 2014; Accepted 24 October 2014

KEY WORDS: shallow water; finite volume; hydrodynamics; partial differential equations; differential equations; verification

1. INTRODUCTION

The shallow water equations (SWE) are of great importance in many application areas, such as flood [1] or tsunami simulations [2] in urban and rural areas, in which waves propagate with a horizontal length scale much greater than the vertical length scale ('shallow waves'). Floods may produce enormous economic damage and human casualties, which have been recently reported to increase because of a number of reasons [3, 4]. In order to minimize the adverse effects of floods, flood mitigation measures are needed, such as adjusting regional planning, constructing levees and polders, establishing evacuation plans, and issuing timely flood warnings once the flood is imminent. All of these tasks rely on accurate and fast simulations of the flood wave propagation based on the SWE. In this paper, we are mainly interested in large-scale flood simulations for which the main challenge is the simulation time (Figure 1).

In recent times, flood events have been reported to occur more frequently [4]. Moreover, their relation to climate change has been seen to embody emerging spatio-temporal features stemming from nonlinear landscape climate dynamics [5]. These floods can contaminate the soil and our water sources, not to mention the human casualties and the financial costs of the caused damages. For this reason, we have to be well prepared and be able to act in time to minimize damages and losses.

*Correspondence to: Zsolt Horváth, Vienna University of Technology, A-1040 Vienna, Karlsplatz 13/222, Austria.
†E-mail: horvath@waterresources.at

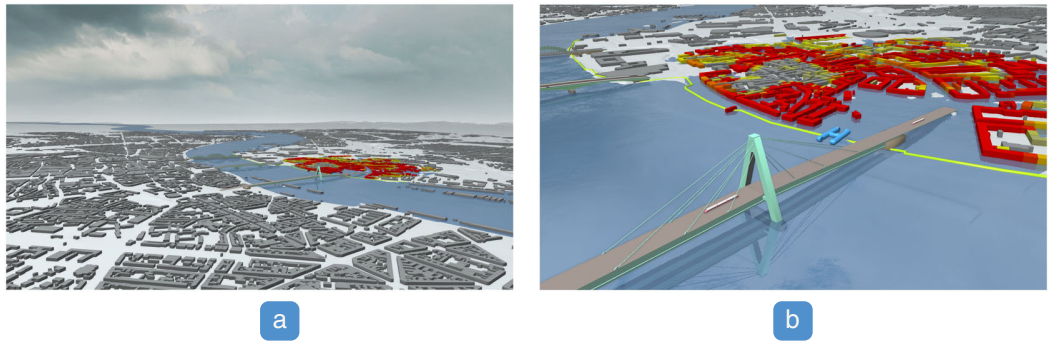

Figure 1. Real-world large-scale simulations of a breach in an urban area in Cologne, Germany. (a) Distant view of the city. (b) Closer view of the flooded area.

The SWE serve as a fundamental and efficient tool for simulating floods and creating protection plans for such catastrophic events. Waser *et al*. [6] present an integrated solution based on the SWE and on multidimensional, time-dependent ensemble simulations of incident scenarios and protective measures. They provide scalable interfaces that facilitate and accelerate setting up multiple time-varying parameters for generating a pool of pre-cooked scenarios.

Shallow water waves are described by the Saint-Venant system [7, 8] in which the motion of the fluid is introduced by the gravity. The equations are derived from depth-integrating the Navier–Stokes equations [9]. This leads to a vertically lumped description of the wave propagation, which assumes invariance in fluid properties with depth. If the fluid is stratified, that is, features vertical layers with different properties (e.g., temperature and density), a system of multiple level SWE (e.g., [10, 11]) can be used with as many levels as there are the layers in the stratified fluid. In this paper, we focus on single-layer shallow waves. Note that the framework can be applied to multiple-level systems.

We are interested in a robust and fast numerical method for the Saint-Venant system of the SWE. We begin with a brief overview and discuss the most important details, which are essential to completely understand the system and the proposed numerical scheme.

The two-dimensional shallow water waves can be described by the following Saint-Venant system [12]:

$$\underbrace{\begin{bmatrix} h \\ hu \\ hv \end{bmatrix}_t}_{\text{conserved variables}} + \underbrace{\begin{bmatrix} hu \\ hu^2 + \frac{1}{2}gh^2 \\ huv \end{bmatrix}_x + \begin{bmatrix} hv \\ huv \\ hv^2 + \frac{1}{2}gh^2 \end{bmatrix}_y}_{\text{flux functions}} = \underbrace{\begin{bmatrix} 0 \\ -ghB_x \\ -ghB_y \end{bmatrix}}_{\text{source terms}}, \tag{1}$$

where h represents the water height, hu is the discharge along the x-axis, hv is the discharge along the y-axis, u and v are the average flow velocities, g is the gravitational constant, and B is the bathymetry (Figure 4a). Subscripts represent partial derivatives, that is, $\mathbf{U}_t$ stands for $\frac{\partial U}{\partial t}$. In vector form, the system can be written down as

$$\mathbf{U}_t + \mathbf{F}(\mathbf{U}, B)_x + \mathbf{G}(\mathbf{U}, B)_y = \mathbf{S}(\mathbf{U}, B), \tag{2}$$

where $\mathbf{U} = [h, hu, hv]$ is the vector of conserved variables, $\mathbf{F}$ and $\mathbf{G}$ are flux functions, and $\mathbf{S}$ represents the source term function.

The method should be accurate on smooth parts of the solution and should not create spurious oscillations near discontinuities, that is, at the dry/wet boundaries. These equations accurately capture both steady-states and quasi-steady flows [8, 13] in which the flux gradients are balanced by the

DOI: 10.1002/fld

source terms. Well-balanced numerical schemes have to be capable of exactly balancing the source terms and numerical fluxes so that the 'lake at rest' steady states are preserved:

$$u = 0, \quad v = 0, \quad w := h + B = \text{Const.}, \tag{3}$$

where w is the total elevation of the water surface. When $h = 0$, the previous state can be reduced to the 'dry lake' steady state:

$$hu = 0, \quad hv = 0, \quad h = 0, \tag{4}$$

which means that no water is present, and the discharges are also zero. A good numerical scheme should be able to exactly preserve both 'lake at rest' and 'dry lake' steady states as well as their combinations. The methods that exactly preserve these solutions are termed 'well-balanced' [14–21]. Therefore, an ideal method should be well balanced in the sense that fluxes and source terms balance exactly, and they result in zero velocities for 'lake at rest' cases.

The simulation of water waves is particularly challenging near dry areas. Standard numerical methods may fail at the dry/wet fronts and produce negative water heights. If the water height becomes negative after the time integration, the whole computation breaks down. All computed water heights must be non-negative. To accomplish this, various positivity-preserving methods are available [8, 14, 22–24]. The last major requirement is the stability of the scheme. In general, to fulfill this requirement, the Courant-Friedrichs-Lewy (CFL) condition [23, 25, 26] is applied. The CFL condition allows for each wave to travel at most one quarter of a grid cell per time step thus limiting the propagation of the information by limiting the time step.

In this paper, we present a new grid-based, central-upwind scheme that satisfies the aforementioned criteria. Following a new reconstruction of the water surface and the draining time step technique [27], we develop a well-balanced, positivity-preserving scheme for the dry/wet fronts. The new method is two dimensional, which makes it suitable for real-world flood simulations by overcoming limitations of one-dimensional schemes. Furthermore, the scheme is well balanced at the partially flooded cells. This allows for longer time steps, which results in shorter simulation run time. We point out that our new two-dimensional scheme is not a direct dimension-by-dimension extension of the one-dimensional scheme presented by Bollerman *et al*. [14], because the latter does not contain some terms that appear only in the two-dimensional scheme. Our two-dimensional scheme is more than a juxtaposition of two one-dimensional schemes.

The paper is structured as follows. In Section 2, we discuss the existing solutions and their drawbacks. In Section 3, we show how to discretize the SWE on a regular grid. In Section 4, we describe the water surface reconstruction at partially flooded cells. In Section 5, we prove the positivity-preserving property of the scheme with the new reconstruction and demonstrate the application of the draining time step technique. In Section 6, we present the evaluation of the proposed scheme. The scientific contributions of the proposed scheme span from fundamental numerical developments to an added practical value to engineering, environmental, and hazard prevention applications. The paper thus contributes with the following key points:

- a physically consistent solution;
- no numerical artifacts at the boundaries;
- two to ten times faster than previous schemes;
- evaluation on two large-scale, real-world scenarios relevant for society (urban and rural flooding);
- an improved numerical scheme for the SWE, based on the two-dimensional reconstruction at the dry/wet boundaries;
- well-balanced states at the dry/wet boundaries in partially flooded cells;
- application of the draining time step technique to preserve non-negative water heights while advancing the solution in time;
- avoiding spurious high velocities at the dry/wet boundaries;
- validation against an analytical solution.

DOI: 10.1002/fld

2. RELATED WORK

There are many schemes available in the literature that satisfy some of the criteria listed in the previous section. For other types of problems (including smooth phenomena, i.e., the formation of eddies [28, 29]), higher-order schemes [19, 21] may be required. We are interested in urban and rural flood simulations, hence, we focus on the second-order schemes that produce sufficiently accurate results for these problems.

In the numerical treatment of the SWE, the spatial domain is discretized. For this purpose, one can use a structured or an unstructured mesh. Most of the numerical schemes developed for the Saint-Venant system are based on the Eulerian approach [15]. This approach uses fixed points in space (grid points) where the fluid properties are evaluated. In general, a uniform rectangular mesh or a triangular mesh is used for this purpose [23]. The second approach is called Lagrangian, where the fluid is being tracked as it flows through space. This is a particle-based approximation of the fluid flow, where each fluid element or particle stores its own properties (e.g., mass, velocity, and position).

We are interested in a two-dimensional, well-balanced, positivity-preserving scheme discretized on a regular rectangular mesh, which is often referred to as regular grid. The scheme has to be able to handle dry and near dry states and solve accurately and efficiently problems characterized by strong discontinuities (e.g., dam breaks and flood breaches).

Kurganov and Levy [8] introduce a second-order scheme using discretization on a regular grid. They propose to use a different reconstruction of the water surface in near dry areas than in the wet zones. The resulting scheme is not well-balanced and violates mass conservation. Furthermore, spurious waves may emerge in the shoal zones. The technique assumes a continuous bathymetry, but a straightforward sampling of a discontinuous bathymetry can result in steep gradients of the bathymetry approximation. This will affect the CFL number [25], restricting the time steps toward very small values.

Kurganov and Petrova [23] improve the previous work by supporting a discontinuous bathymetry. They describe a reconstruction adjustment for the partially flooded cells, where values of the water depth become negative at the integration points. If the reconstructed water slope creates negative values at the integration points, they adjust the steepness of the slope so that the negative values become zero. Their correction solves the positivity problem by raising and lowering the water level at the left and right side of the cell according to the bathymetry function. This guarantees that all water heights are non-negative. However, at the partially flooded cells, this can lead to large errors for small water heights, and the flow velocity will grow smoothly in these formerly dry areas. Another issue related to this modification is that the water climbs up on the shores at the dry/wet boundaries. Finally, if a cell becomes wet, it will almost never be completely dry again.

Bollermann *et al*. [14] extend the Kurganov and Petrova [23] scheme and achieves well-balanced states in the partially flooded cells by constructing an alternative correction procedure, which is similar to the reconstruction used by Tai [30]. However, this modification works only for one dimension and can lead to infinitely small time steps. To overcome this time step limitation, Bollermann uses the draining time technique introduced in [27]. This scheme is only one-dimensional, and it is not sufficient for our simulations.

Apart from the regular grid-based schemes, various techniques exist for structured and unstructured meshes. For instance, Bryson *et al*. [31] develop a well-balanced positivity-preserving numerical scheme for triangular grids. This scheme can be applied to models with discontinuous bathymetry and irregular channel widths. Even though the method can be well adopted to irregular topographies, its implementation is more complex, and it has higher computational requirements than the scheme we introduce in this paper.

3. TWO-DIMENSIONAL CENTRAL-UPWIND SCHEME

Our work is based on the two-dimensional, central-upwind scheme of Kurganov and Petrova [23]. In this section, we describe this technique for solving the Saint-Venant system of SWE on uniform grids. Table I explains the notations used throughout the text.

DOI: 10.1002/fld

Table I. Notations for the numerical scheme.

$\mathbf{V}$	$\triangleq$	vector (e.g., $\mathbf{U} = [h, hu, hv]$)
$\bar{\mathbf{U}}$	$\triangleq$	cell average values
$\tilde{\mathbf{U}}$	$\triangleq$	approximated values
$\mathbf{U}_{j,k}$	$\triangleq$	vector at position $[j, k]$
$\mathbf{U}^{\pm}$	$\triangleq$	left-sided and right-sided point values
$\mathbf{U}^n$	$\triangleq$	vector at time t_n ($\mathbf{U}^n = \mathbf{U}(t_n)$)
$\mathbf{H}^{\mathbf{x}}$	$\triangleq$	central-upwind flux function in x-dimension
$\mathbf{H}^{(1)}$	$\triangleq$	first element of vector $\mathbf{H} = [\mathbf{H}^{(1)}, \mathbf{H}^{(2)}, \mathbf{H}^{(3)}]$
v	$\triangleq$	variable
v^*	$\triangleq$	special variable
$B_{j,k}$	$\triangleq$	value at position $[j, k]$

LEGEND

$\bar{hu}$ discharge in x-dimension
$\bar{hv}$ discharge in y-dimension
Δx cell width in x-dimension
Δy cell width in y-dimension
cell interface midpoints
cell vertices
cell center (cell average)

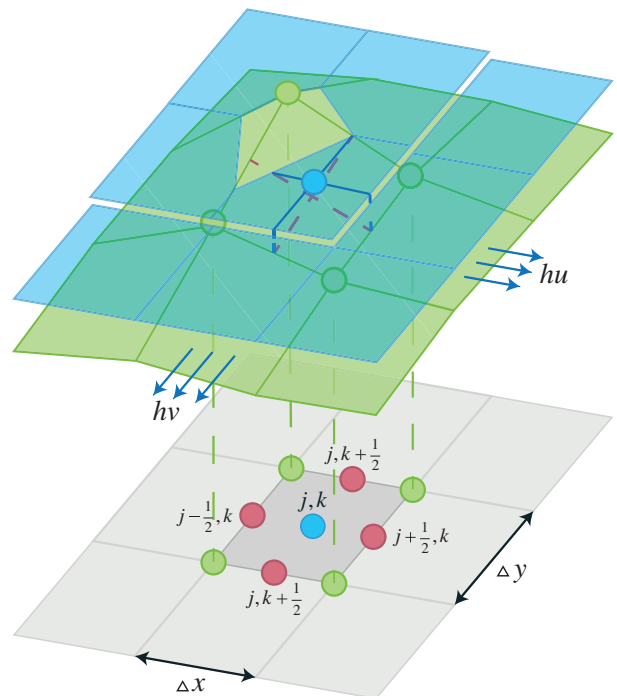

Figure 2. Two-dimensional grid-based representation of average water elevations $\bar{w}$, discharges $\bar{hu}$, $\bar{hv}$, and bathymetry B. For a bilinear reconstruction, the cell averages coincide with the values at the cell centers. The bathymetry is approximated by its values at the cell vertices. In this figure, the middle cell is fully flooded in the y-dimension while only partially flooded in the x-dimension. Waterlines are represented by the blue lines and red dashed lines mark the bathymetry slopes in both dimensions.

We introduce a uniform grid $x_\alpha := \alpha\Delta x$ and $y_\beta := \beta\Delta y$, where Δx and Δy are small spatial scales (Figure 2), and we denote by $C_{j,k}$ the finite volume cells $C_{j,k} := \left[x_{j-\frac{1}{2}}, x_{j+\frac{1}{2}}\right] \times \left[y_{k-\frac{1}{2}}, y_{k+\frac{1}{2}}\right]$. The central-upwind semi-discretization (discretized only in space, while time remains continuous) of Equation (2) can be written down as the following system of time-dependent, ordinary differential equations [8, 32]:

$$\frac{d}{dt}\bar{\mathbf{U}}_{j,k}(t) = -\frac{\mathbf{H}^x_{j+\frac{1}{2},k}(t) - \mathbf{H}^x_{j-\frac{1}{2},k}(t)}{\Delta x} - \frac{\mathbf{H}^y_{j,k+\frac{1}{2}}(t) - \mathbf{H}^y_{j,k-\frac{1}{2}}(t)}{\Delta y} + \bar{\mathbf{S}}_{j,k}(t), \tag{5}$$

DOI: 10.1002/fld

where $\mathbf{H}^x_{j\mp\frac{1}{2},k}$ and $\mathbf{H}^y_{j,k\mp\frac{1}{2}}$ are the central-upwind fluxes, and $\bar{\mathbf{S}}_{j,k}$ is an appropriate discretization of the cell averages of the source term

$$\bar{\mathbf{S}}_{j,k}(t) \approx \frac{1}{\Delta x \Delta y} \iint\limits_{C_{j,k}} \mathbf{S}(\mathbf{U}(x,y,t), B(x,y))dxdy, \tag{6}$$

which in our case only contains the bed source term. The friction term is omitted for simplification purposes without loss of generality.

We start by replacing the bathymetry function $B(x,y)$ with its continuous, piecewise bilinear approximation $\tilde{B}(x,y)$, which at each cell $C_{j,k}$ is given by a bilinear form. The vertex values $B_{j\pm\frac{1}{2},k\pm\frac{1}{2}}$ of the cell $C_{j,k}$ are computed based on the continuous bathymetry function (Figure 3).

The average value of $\tilde{B}$ over the cell $C_{j,k}$ is equal to its value $B_{j,k}$ at the center of this cell. Furthermore, it is equal to the average value of the values at cell interface midpoints:

$$B_{j,k} = \frac{1}{4}\left(B_{j+\frac{1}{2},k} + B_{j-\frac{1}{2},k} + B_{j,k+\frac{1}{2}} + B_{j,k-\frac{1}{2}}\right). \tag{7}$$

Further details on the piecewise bilinear approximation of the bathymetry can be found in [23].

Using the approximated bathymetry values at cell interface midpoints (Figure 4a–b), we have the discretized source terms in the following form [8, 23]:

$$\bar{\mathbf{S}}^{(1)}_{j,k}(t) := 0, \tag{8}$$

$$\bar{\mathbf{S}}^{(2)}_{j,k}(t) := -g\bar{h}_{j,k}\frac{B_{j+\frac{1}{2},k} - B_{j-\frac{1}{2},k}}{\Delta x}, \tag{9}$$

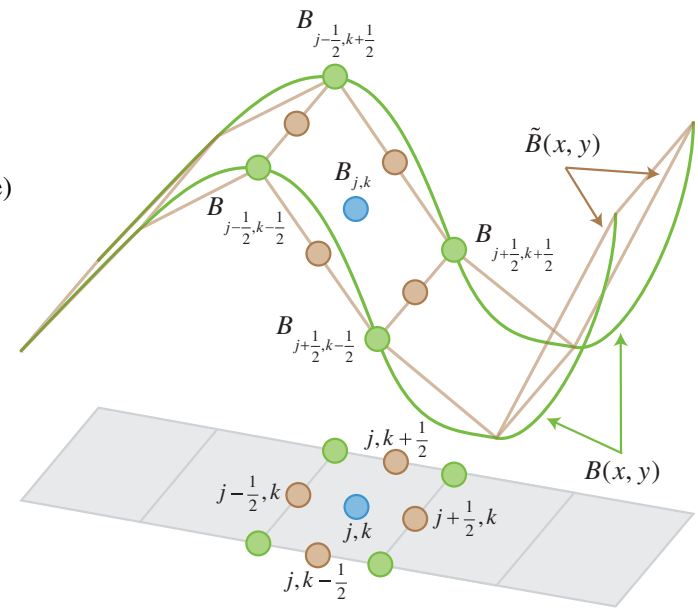

Figure 3. Continuous bathymetry function $B(x,y)$ (green) and its piecewise linear approximation $\tilde{B}(x,y)$ (brown dots). The approximated function values equal to the continuous ones at the cell vertices (green dots). The cell average value (blue dot) equals both to the average value of the vertex values (green dots) and to the average value of the values at the cell interface midpoints (brown dots).

DOI: 10.1002/fld

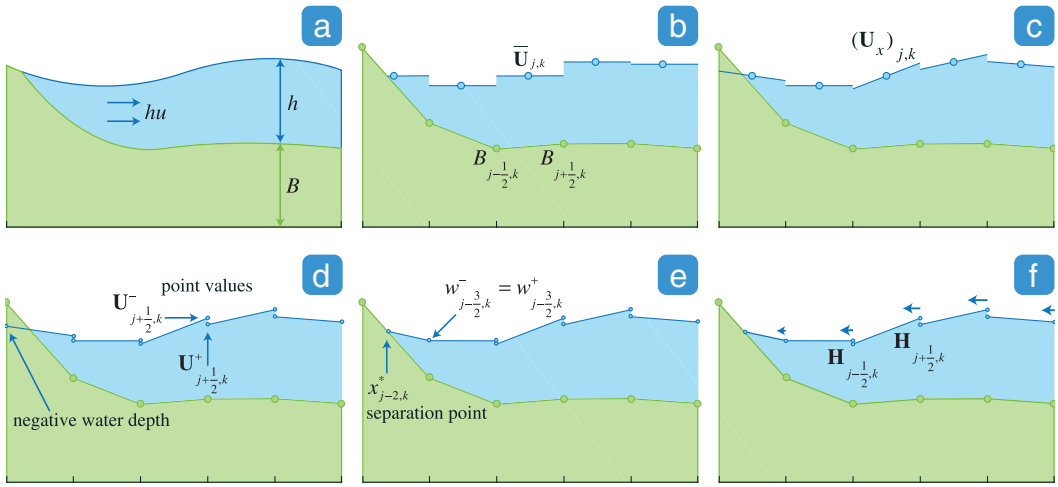

Figure 4. (a) Schematic view of a shallow water flow at a dry/wet boundary and definition of the variables. (b) Conserved variables $\mathbf{U}$ are discretized as cell averages $\bar{\mathbf{U}}_{j,k}$. The bathymetry function B is computed at cell interface midpoints. (c) Slopes U_x are reconstructed using the minmod flux limiter. (d) Left-sided and right-sided point values are computed at cell interface midpoints. (e) At the almost dry cells, the slope is modified to avoid negative water heights, and a separation point is generated. (f) Fluxes are computed using the central-upwind flux function at each cell interface.

$$\bar{\mathbf{S}}^{(3)}_{j,k}(t) := -g\bar{h}_{j,k}\frac{B_{j,k+\frac{1}{2}} - B_{j,k-\frac{1}{2}}}{\Delta y}, \tag{10}$$

where we omit the time dependence t on the right hand side for simplification reasons without loss of generality, as we do in the following equations.

On the next step, we reconstruct the slope of the water surface in the cells (Figure 4c). The reconstruction of the left-sided and right-sided point values (Figure 4d) is second-order accurate if the approximate values of the derivatives $(\mathbf{U}_x)_{j,k}$ and $(\mathbf{U}_y)_{j,k}$ are at least first-order componentwise approximations of $\mathbf{U}_x(x_j, y_k)$ and $\mathbf{U}_y(x_j, y_k)$. To preserve second-order accuracy, these values are computed using a non-linear limiter. In addition, to ensure non-oscillatory reconstruction and to avoid oscillation artifacts in the numerical solution, we use the generalized minmod limiter [33–36]:

$$\begin{aligned}
(\mathbf{U}_x)_{j,k} &= \text{minmod}\left(\theta\frac{\bar{\mathbf{U}}_{j,k} - \bar{\mathbf{U}}_{j-1,k}}{\Delta x}, \frac{\bar{\mathbf{U}}_{j+1,k} - \bar{\mathbf{U}}_{j-1,k}}{2\Delta x}, \theta\frac{\bar{\mathbf{U}}_{j+1,k} - \bar{\mathbf{U}}_{j,k}}{\Delta x}\right),\\
(\mathbf{U}_y)_{j,k} &= \text{minmod}\left(\theta\frac{\bar{\mathbf{U}}_{j,k} - \bar{\mathbf{U}}_{j,k-1}}{\Delta y}, \frac{\bar{\mathbf{U}}_{j,k+1} - \bar{\mathbf{U}}_{j,k-1}}{2\Delta y}, \theta\frac{\bar{\mathbf{U}}_{j,k+1} - \bar{\mathbf{U}}_{j,k}}{\Delta y}\right),
\end{aligned} \tag{11}$$

where $\theta \in [1, 2]$ is a parameter used to affect the numerical viscosity of the scheme. As suggested in [8], we set $\theta = 1.3$, which is close to the optimal value. The minmod function is defined as

$$\text{minmod}(z_1, z_2, z_3) := \begin{cases} \min_j\{z_j\}, & \text{if } z_j > 0 \quad \forall j,\\ \max_j\{z_j\}, & \text{if } z_j < 0 \quad \forall j,\\ 0, & \text{otherwise,}\end{cases} \tag{12}$$

and is applied in a componentwise manner to all three elements $\left[\bar{w}, \bar{hu}, \bar{hv}\right]$ of vector $\bar{\mathbf{U}}$, where we reconstruct water levels $\bar{w}$ instead of water heights $\bar{h}$. Other non-linear limiters can be found in the literature [33–39].

DOI: 10.1002/fld

The values $\mathbf{U}^{\pm}_{j+\frac{1}{2},k} = \left(w^{\pm}_{j+\frac{1}{2},k}, hu^{\pm}_{j+\frac{1}{2},k}, hv^{\pm}_{j+\frac{1}{2},k}\right)$ and $\mathbf{U}^{\pm}_{j,k+\frac{1}{2}} = \left(w^{\pm}_{j,k+\frac{1}{2}}, hu^{\pm}_{j,k+\frac{1}{2}}, hv^{\pm}_{j,k+\frac{1}{2}}\right)$ are referred to as the left-sided and right-sided point values (Figure 4d). They are obtained by the piecewise linear reconstruction $\tilde{\mathbf{U}} \equiv (\tilde{w}, \tilde{hu}, \tilde{hv})$ for $\mathbf{U}$ at cell interface midpoints $\left[x_{j+\frac{1}{2}}, y_k\right]$ and $\left[x_j, y_{k+\frac{1}{2}}\right]$,

$$\tilde{\mathbf{U}}(x,y) := \bar{\mathbf{U}}_{j,k} + (\mathbf{U}_x)_{j,k}(x - x_j) + (\mathbf{U}_y)_{j,k}(y - y_k), \quad (x,y) \in C_{j,k}. \tag{13}$$

For cell $C_{j,k}$, we get the following four vectors describing the reconstructed point values:

$$\mathbf{U}^{-}_{j+\frac{1}{2},k} = \mathbf{U}_{j,k} + \frac{\Delta x}{2}(\mathbf{U}_x)_{j,k}, \quad \mathbf{U}^{+}_{j-\frac{1}{2},k} = \mathbf{U}_{j,k} - \frac{\Delta x}{2}(\mathbf{U}_x)_{j,k},$$
$$\mathbf{U}^{-}_{j,k+\frac{1}{2}} = \mathbf{U}_{j,k} + \frac{\Delta y}{2}(\mathbf{U}_y)_{j,k}, \quad \mathbf{U}^{+}_{j,k-\frac{1}{2}} = \mathbf{U}_{j,k} - \frac{\Delta y}{2}(\mathbf{U}_y)_{j,k}.$$

We note that the reconstruction procedure in Equations (11)–(13) might produce negative water heights in the partially flooded cells [14, 23] (Figure 4d). Therefore, we need to correct them (Figure 4e). The correction technique proposed in [23] violates the well-balanced property of the scheme and causes high velocities in these areas. Hence, we use a modified correction that has been first derived for the one-dimensional case [14]. Ensuring both well-balanced and positivity-preserving properties for the two-dimensional version is not straightforward. Our new reconstruction affects only the partially flooded cells while maintaining the well-balanced property of the scheme. The derivation of the two-dimensional version is presented in Section 4.

Using the point values, we can calculate the fluxes needed for the computation of the next time step. The central-upwind numerical fluxes $\mathbf{H}^{x}_{j+\frac{1}{2},k}$ and $\mathbf{H}^{y}_{j,k+\frac{1}{2}}$ (Figure 4f) are given by

$$\mathbf{H}^{x}_{j+\frac{1}{2},k} = \frac{a^{+}_{j+\frac{1}{2},k}\mathbf{F}\left(\mathbf{U}^{-}_{j+\frac{1}{2},k}, B_{j+\frac{1}{2},k}\right) - a^{-}_{j+\frac{1}{2},k}\mathbf{F}\left(\mathbf{U}^{+}_{j+\frac{1}{2},k}, B_{j+\frac{1}{2},k}\right)}{a^{+}_{j+\frac{1}{2},k} - a^{-}_{j+\frac{1}{2},k}} + \frac{a^{+}_{j+\frac{1}{2},k}a^{-}_{j+\frac{1}{2},k}}{a^{+}_{j+\frac{1}{2},k} - a^{-}_{j+\frac{1}{2},k}}\left[\mathbf{U}^{+}_{j+\frac{1}{2},k} - \mathbf{U}^{-}_{j+\frac{1}{2},k}\right], \tag{14}$$

$$\mathbf{H}^{y}_{j,k+\frac{1}{2}} = \frac{b^{+}_{j,k+\frac{1}{2}}\mathbf{G}\left(\mathbf{U}^{-}_{j,k+\frac{1}{2}}, B_{j,k+\frac{1}{2}}\right) - b^{-}_{j,k+\frac{1}{2}}\mathbf{G}\left(\mathbf{U}^{+}_{j,k+\frac{1}{2}}, B_{j,k+\frac{1}{2}}\right)}{b^{+}_{j,k+\frac{1}{2}} - b^{-}_{j,k+\frac{1}{2}}} + \frac{b^{+}_{j,k+\frac{1}{2}}b^{-}_{j,k+\frac{1}{2}}}{b^{+}_{j,k+\frac{1}{2}} - b^{-}_{j,k+\frac{1}{2}}}\left[\mathbf{U}^{+}_{j,k+\frac{1}{2}} - \mathbf{U}^{-}_{j,k+\frac{1}{2}}\right], \tag{15}$$

where we use the following flux notations:

$$\mathbf{F}(\mathbf{U}, B) := \left[hu, \tfrac{(hu)^2}{w-B} + \tfrac{1}{2}\mathrm{g}(w-B)^2, huv\right]^T \tag{16}$$

$$\mathbf{G}(\mathbf{U}, B) := \left[hv, huv, \tfrac{(hv)^2}{w-B} + \tfrac{1}{2}\mathrm{g}(w-B)^2\right]^T. \tag{17}$$

DOI: 10.1002/fld

We note that the central-upwind flux is a direct generalization of the well-known Harten–Lax–van Leer flux [40, 41].

The speed values $a^{\pm}_{j+\frac{1}{2},k}$ and $b^{\pm}_{j+\frac{1}{2},k}$ of propagation [32] are obtained using the eigenvalues of the Jacobian $\frac{\partial \mathbf{F}}{\partial \mathbf{U}}$ as follows:

$$a^{+}_{j+\frac{1}{2},k} = \max\left\{u^{-}_{j+\frac{1}{2},k} + \sqrt{\mathrm{g}h^{-}_{j+\frac{1}{2},k}}, u^{+}_{j+\frac{1}{2},k} + \sqrt{\mathrm{g}h^{+}_{j+\frac{1}{2},k}}, 0\right\} \tag{18}$$

$$a^{-}_{j+\frac{1}{2},k} = \min\left\{u^{-}_{j+\frac{1}{2},k} - \sqrt{\mathrm{g}h^{-}_{j+\frac{1}{2},k}}, u^{+}_{j+\frac{1}{2},k} - \sqrt{\mathrm{g}h^{+}_{j+\frac{1}{2},k}}, 0\right\} \tag{19}$$

$$b^{+}_{j,k+\frac{1}{2}} = \max\left\{v^{-}_{j,k+\frac{1}{2}} + \sqrt{\mathrm{g}h^{-}_{j,k+\frac{1}{2}}}, v^{+}_{j,k+\frac{1}{2}} + \sqrt{\mathrm{g}h^{+}_{j,k+\frac{1}{2}}}, 0\right\} \tag{20}$$

$$b^{-}_{j,k+\frac{1}{2}} = \min\left\{v^{-}_{j,k+\frac{1}{2}} - \sqrt{\mathrm{g}h^{-}_{j,k+\frac{1}{2}}}, v^{+}_{j,k+\frac{1}{2}} - \sqrt{\mathrm{g}h^{+}_{j,k+\frac{1}{2}}}, 0\right\} \tag{21}$$

Using the semi-discrete Equation(5) together with the forward Euler temporal discretization, we obtain the discrete equation for the computation of the next time step as

$$\bar{\mathbf{U}}^{n+1}_{j,k} = \bar{\mathbf{U}}^{n}_{j,k} - \lambda\left(\mathbf{H}^{x}_{j+\frac{1}{2},k} - \mathbf{H}^{x}_{j-\frac{1}{2},k}\right) - \mu\left(\mathbf{H}^{y}_{j,k+\frac{1}{2}} - \mathbf{H}^{y}_{j,k-\frac{1}{2}}\right), \tag{22}$$

where $\lambda := \Delta t/\Delta x$, $\mu := \Delta t/\Delta y$, and the numerical fluxes $\mathbf{H}^{x}_{j\pm\frac{1}{2},k}$ and $\mathbf{H}^{y}_{j,k\pm\frac{1}{2}}$ are evaluated at time $t = t^n$. In order to keep the numerical integration stable, the time step size Δt has to satisfy the CFL condition:

$$\Delta t \leqslant \mathbf{CFL}\min\left\{\frac{\Delta x}{a}, \frac{\Delta y}{b}\right\}, \tag{23}$$

where $\mathbf{CFL} := \frac{1}{4}$ for the two-dimensional scheme, and a and b are given by

$$a := \max_{j,k}\left\{\max\left\{a^{+}_{j+\frac{1}{2},k}, -a^{-}_{j+\frac{1}{2},k}\right\}\right\}, \quad b := \max_{j,k}\left\{\max\left\{b^{+}_{j,k+\frac{1}{2}}, -b^{-}_{j,k+\frac{1}{2}}\right\}\right\}. \tag{24}$$

4. RECONSTRUCTION AT PARTIALLY FLOODED CELLS

The central-upwind scheme described in the previous section may produce negative water values in the partially flooded cells on the reconstruction step (Figure 5a). Even if the total amount of water in the cell is positive ($\bar{w}_{j,k} > B_{j,k}$), the water level in the cell may intersect the bathymetry ($\bar{w}_{j,k} < B_{j-\frac{1}{2},k}$), and thus, the point value at the cell interface becomes negative ($h_{j-\frac{1}{2},k} < 0$). One could try replacing the first-order, piecewise, constant reconstruction with a higher order, piecewise, linear reconstruction, but it will not guarantee positive reconstructed point values at the cell interfaces. Therefore, we need to correct these point values. The correction proposed in [23] solves the problem of the negative point values but violates the well-balanced property of the scheme (Figure 5b). Based

DOI: 10.1002/fld

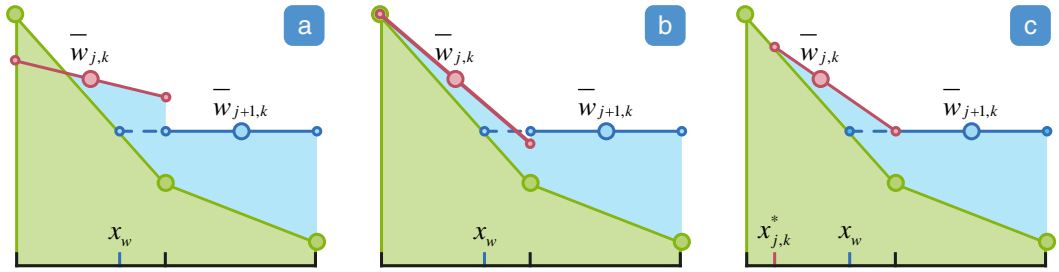

Figure 5. Approximations of the wet/dry front reconstruction. The blue dashed line represents the waterline of the fully flooded cell. (a) Wrong approximation by the piecewise linear reconstruction, which produces a negative water value. (b) Positivity preserving but unbalanced piecewise linear reconstruction. (c) Positivity-preserving and well-balanced piecewise linear reconstruction.

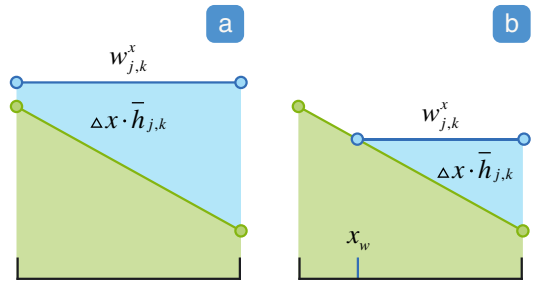

Figure 6. Waterline $w^x_{j,k}$ computation using the conservation of the average water height $\bar{h}_{j,k}$, where $\Delta x \cdot \bar{h}_{j,k}$ equals to the amount of water in the cell. (a) In the fully flooded cell, the waterline does not intersect the bathymetry. (b) In the partially flooded cell, x_w marks the intersection point between the waterline and the bathymetry.

on the modified technique proposed in [14] for the one-dimensional scheme (Figure 5c), we extend this correction for two dimensions.

We assume that at a certain time t, all computed water levels are higher or equal to the bathymetry elevation ($\bar{w}_{j,k} \geqslant B_{j,k}$). In addition, in the piecewise linear reconstruction in Equation (13), we use a non-linear limiter to compute the slopes $(\mathbf{U}_x)_{j,k}$ and $(\mathbf{U}_y)_{j,k}$. We also assume that at an arbitrary partially flooded cell $C_{j,k}$,

$$B_{j-\frac{1}{2},k} > \bar{w}_{j,k} > B_{j+\frac{1}{2},k} \quad \text{or} \quad B_{j,k-\frac{1}{2}} > \bar{w}_{j,k} > B_{j,k+\frac{1}{2}} \tag{25}$$

and that the reconstructed point values of w in cell $C_{j+1,k}$ and $C_{j,k+1}$ satisfy

$$\begin{aligned} &w^+_{j+\frac{1}{2},k} B_{j+\frac{1}{2},k} \quad \text{and} \quad w^-_{j+\frac{3}{2},k} \quad B_{j+\frac{3}{2},k}, \\ &w^+_{j,k+\frac{1}{2}} B_{j,k+\frac{1}{2}} \quad \text{and} \quad w^-_{j,k+\frac{3}{2}} \quad B_{j,k+\frac{3}{2}}. \end{aligned} \tag{26}$$

Symmetric cases can be treated the same way.

We start with computing the water surface $w_{j,k}$ in cell $C_{j,k}$. In order to distinguish between the two dimensions, $w^x_{j,k}$ marks the waterline for the x-dimension and $w^y_{j,k}$ for the y-dimension. The water level is the average elevation of the water surface in a cell. The waterline is a horizontal line which represents the real water surface in a cell computed from the amount of water present in that cell, which means it can differ from the average water elevation. If the cell is fully flooded, we can represent the line by a linear function (Figure 6a). Otherwise, it has to be represented by a piecewise

DOI: 10.1002/fld

linear function, with a separation point $x^*_{j,k}$, which defines the location where the water height becomes zero (Figure 5c). We choose a water height in a way that the volume enclosed between the surface and the bathymetry equals to the amount of water in that cell (Figure 6b). The amount of water in cell $C_{j,k}$ is defined by $\Delta x \cdot \bar{h}_{j,k}$ and $\Delta y \cdot \bar{h}_{j,k}$ for each direction respectively, where $\bar{h}_{j,k} := \bar{w}_{j,k} - B_{j,k}$. These areas can be represented by trapezoids, if the cell is fully filled, or by triangular shapes, if the cell is partially flooded (Figure 6). We note that a cell can be fully flooded in one dimension, while only partially flooded in the other. If cell $C_{j,k}$ is fully flooded, the following conditions hold:

$$\bar{h}_{j,k} \geqslant \frac{\Delta x}{2}|(B_x)_{j,k}|, \quad \bar{h}_{j,k} \geqslant \frac{\Delta y}{2}|(B_y)_{j,k}|, \tag{27}$$

where $\bar{h}_{j,k}$ is the average water height of the cell, $(B_x)_{j,k}$ and $(B_y)_{j,k}$ are the bathymetry slopes in x and y directions. In this case, functions $s^x_{j,k}(x, y)$ and $s^y_{j,k}(x, y)$ represent the water surface for both dimensions:

$$s^x_{j,k}(x, y) = \bar{w}_{j,k}, \quad s^y_{j,k}(x, y) = \bar{w}_{j,k},$$

otherwise the free surface is a continuous piecewise linear function given by

$$s^x_{j,k}(x, y) = \begin{cases} B_{j,k}(x, y), & \text{if } x < x^*_w, \\ w^x_{j,k}, & \text{otherwise,} \end{cases} \quad s^y_{j,k}(x, y) = \begin{cases} B_{j,k}(x, y), & \text{if } y < y^*_w, \\ w^y_{j,k}, & \text{otherwise,} \end{cases}, \tag{28}$$

where x^*_w and y^*_w are the boundary points separating the dry and wet parts in the cell $C_{j,k}$, and $B_{j,k}(x, y)$ is a two-dimensional plane representing the bathymetry approximation in the cell. The boundary separation points can be determined by the following equations:

$$\Delta x^*_w = \sqrt{\frac{2\Delta x \bar{h}_{j,k}}{|(B_x)_{j,k}|}} \quad \Delta y^*_w = \sqrt{\frac{2\Delta y \bar{h}_{j,k}}{|(B_y)_{j,k}|}} \tag{29}$$

where $\Delta x^*_w = x_{j+\frac{1}{2}} - x^*_w$ and $\Delta y^*_w = y_{j+\frac{1}{2}} - y^*_w$. More details on deriving this equation can be found in [14, 42]. The average total elevation of the water surface for the wet/dry cell is then computed as

$$\begin{aligned} w^x_{j,k} &= B_{j,k} + \left(\Delta x^*_w - \frac{\Delta x}{2}\right)|(B_x)_{j,k}| \\ w^y_{j,k} &= B_{j,k} + \left(\Delta y^*_w - \frac{\Delta y}{2}\right)|(B_y)_{j,k}| \end{aligned} \tag{30}$$

Note that if a cell satisfies at least one condition of Equation (27), then it is a partially flooded cell with $\Delta x^*_w < \Delta x$ or $\Delta y^*_w < \Delta y$.

In the following, we discuss the reconstruction of the waterline for the x-dimension. It can be computed analogously for the y-dimension. At this point, we know which cells are partially flooded. For these cells, we modify the reconstruction of the water height h to ensure the well-balanced property. We assign the value of the reconstructed water height of the next fully flooded cell $C_{j+1,k}$ to the value of the same interface at the partially flooded cell $C_{j,k}$, $w^-_{j+\frac{1}{2},k} := w^+_{j+\frac{1}{2},k}$. Using this value and the conservation of the average water height $\bar{h}_{j,k}$, we determine the waterline $w^x_{j,k}$ in cell $C_{j,k}$. This assignment implies that $h^-_{j+\frac{1}{2},k} := w^-_{j+\frac{1}{2},k} - B_{j+\frac{1}{2},k} = w^+_{j+\frac{1}{2},k} - B_{j+\frac{1}{2},k} =: h^+_{j+\frac{1}{2},k}$.

DOI: 10.1002/fld

If the amount of water in cell $C_{j,k}$ is sufficiently large, then $h^+_{j-\frac{1}{2},k} \geqslant 0$ and satisfies

$$\bar{h}_{j,k} = \frac{1}{2}\left(h^-_{j+\frac{1}{2},k} + h^+_{j-\frac{1}{2},k}\right), \tag{31}$$

from which we obtain the total water level $w^+_{j-\frac{1}{2},k} = h^+_{j-\frac{1}{2},k} + B_{j-\frac{1}{2},k}$, and thus, the well-balanced reconstruction for cell $C_{j,k}$ is completed.

If the value of $h^+_{j-\frac{1}{2},k}$ at the other interface computed from the conservation requirement in Equation (31) is negative, we replace the waterline $w^x_{j,k}$ in cell $C_{j,k}$ with two linear pieces. The breaking point between the 'wet' and 'dry' pieces is marked by $x^*_{j,k}$ and is determined by the conservation requirement, which in this case reads

$$\Delta x \cdot \bar{h}_{j,k} = \frac{\Delta x^*_{j,k}}{2} h^-_{j+\frac{1}{2},k}, \tag{32}$$

where

$$\Delta x^*_{j,k} = |x_{j+\frac{1}{2},k} - x^*_{j,k}|.$$

Using the idea from [14] and combining the aforementioned two cases, we obtain the reconstructed value:

$$h^+_{j-\frac{1}{2},k} = \max\left\{0, 2\bar{h}_{j,k} - h^-_{j+\frac{1}{2},k}\right\}. \tag{33}$$

As in [14], we also generalize the definition of $\Delta x^*_{j,k}$ and set

$$\Delta x^*_{j,k} = \Delta x \cdot \min\left\{\frac{2\bar{h}_{j,k}}{h^-_{j+\frac{1}{2},k}}, 1\right\}. \tag{34}$$

The well-balanced reconstruction for the x-dimension is completed. Following this technique, one can easily derive it for the second dimension.

We mentioned that the piecewise linear reconstruction in Equations (12)–(13) does not guarantee the positivity of the point values at the dry/wet fronts; thus, they have to be corrected. This approach only modifies the reconstructed water values $\tilde{w}^\pm_{j\pm\frac{1}{2},k}$. Next, as in [14], we summarize the possible cases of the modified reconstruction, where $\bar{w}_{j,k}$ is the average water level in the cell, $\tilde{w}^\pm_{j\pm\frac{1}{2},k}$ are the point values reconstructed using the minmod flux limiter in Equation (11), and $w^\pm_{j\pm\frac{1}{2},k}$ are the corrected values:

Case 1. If $\bar{w}_{j,k} > B_{j-\frac{1}{2},k}$ and $\bar{w}_{j,k} > B_{j+\frac{1}{2},k}$, then cell $C_{j,k}$ is fully flooded.

1A. If $\tilde{w}^+_{j-\frac{1}{2},k} \geqslant B_{j-\frac{1}{2},k}$ and $\tilde{w}^-_{j+\frac{1}{2},k} \geqslant B_{j+\frac{1}{2},k}$, the cell is flooded, and we set $w^\pm_{j+\frac{1}{2},k} := \tilde{w}^\pm_{j+\frac{1}{2},k}$ (Figure 7a).

1B. Otherwise, as in [23], we redistribute the water (Figure 7b) in the following ways:

$$\text{If} \quad \tilde{w}^+_{j-\frac{1}{2},k} < B_{j-\frac{1}{2},k}, \quad \text{then set} \quad (w_x)_{j,k} := \frac{\bar{w}_{j,k} - B_{j-\frac{1}{2},k}}{\Delta x/2},$$

$$\Longrightarrow \quad w^-_{j+\frac{1}{2},k} = 2\bar{w}_{j,k} - B_{j-\frac{1}{2},k}, \quad w^+_{j-\frac{1}{2},k} = B_{j-\frac{1}{2},k},$$

DOI: 10.1002/fld

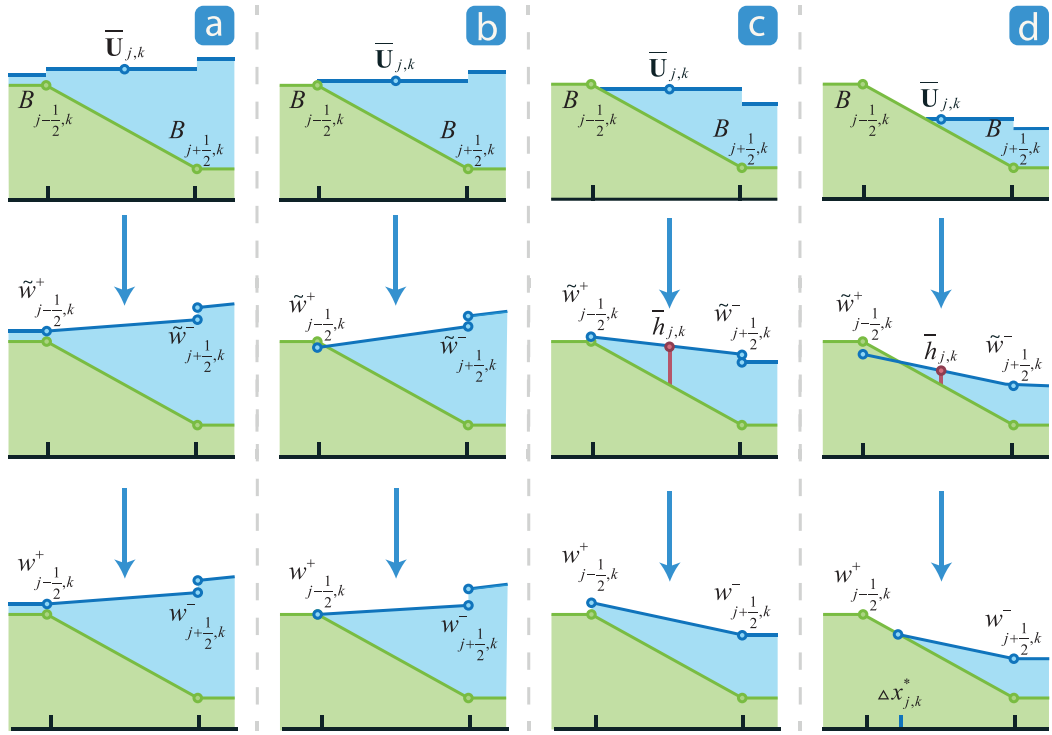

Figure 7. Illustrations of reconstruction cases for the wet/dry fronts. The upper row shows the average water levels in the cells, the row in the middle shows the reconstructed point values, and the bottom row shows the modified point values. (a) The amount of water is enough to fill the cell, the reconstruction is correct. (b) The amount of water is enough to fill the cell, but a negative point value was produced, therefore, we set it to zero, and the value on the right side requires correction because of the conservation criterion. (c) The cell is partially flooded, and after equalizing the water height between the current and the next fully flooded cell, both values become positive. (d) The cell is partially flooded, and there is not enough water to fill it after the equalization.

and symmetrically,

$$\text{if} \quad \tilde{w}^-_{j+\frac{1}{2},k} < B_{j+\frac{1}{2},k}, \quad \text{then set} \quad (w_x)_{j,k} := \frac{B_{j+\frac{1}{2},k} - \bar{w}_{j,k}}{\Delta x/2},$$

$$\Longrightarrow \; w^-_{j+\frac{1}{2},k} = B_{j+\frac{1}{2},k}, \quad w^+_{j-\frac{1}{2},k} = 2\bar{w}_{j,k} - B_{j+\frac{1}{2},k}.$$

Case 2. If $B_{j-\frac{1}{2},k} > \bar{w}_{j,k} > B_{j+\frac{1}{2},k}$, then cell $C_{j,k}$ is possibly partially flooded.

2A. If $\tilde{w}^+_{j+\frac{1}{2},k} > B_{j+\frac{1}{2},k}$ and $\tilde{w}^-_{j+\frac{3}{2},k} > B_{j+\frac{3}{2},k}$, then cell $C_{j+1,k}$ is fully flooded and $w^+_{j+\frac{1}{2},k} = \tilde{w}^+_{j+\frac{1}{2},k}$. We set $w^-_{j+\frac{1}{2},k} := w^+_{j+\frac{1}{2},k}$ and $h^-_{j+\frac{1}{2},k} := w^-_{j+\frac{1}{2},k} - B_{j+\frac{1}{2},k}$.

2A1. If $2\bar{h}_{j,k} - h^-_{j+\frac{1}{2},k} \geqslant 0$, then the amount of water in cell $C_{j,k}$ is sufficiently large, and we set $h^+_{j-\frac{1}{2},k} = 2\bar{h}_{j,k} - h^-_{j+\frac{1}{2},k}$, so $w^+_{j-\frac{1}{2},k} = h^+_{j-\frac{1}{2},k} + B_{j-\frac{1}{2},k}$ (Figure 7c).

2A2. Otherwise set $h^-_{j+\frac{1}{2},k} = 0$, $w^+_{j-\frac{1}{2},k} = B_{j-\frac{1}{2},k}$ and $\Delta x^*_{j,k}$ as in Equation (34) (Figure 7d).

2B. Otherwise set $h^-_{j+\frac{1}{2},k} := w_{j,k} - B_{j+\frac{1}{2},k}$ and $\Delta x^*_{j,k} := \Delta x^*_w$. This situation is not generic and may occur only in the under-resolved computations [14].

DOI: 10.1002/fld

Case 3. $B_{j-\frac{1}{2},k} < \bar{w}_{j,k} < B_{j+\frac{1}{2},k}$ is analogous to Case 2.

The correction cases for the second dimension can be derived analogously by changing indices from $j-\frac{1}{2},k$ and $j+\frac{1}{2},k$ to $j,k-\frac{1}{2}$ and $j,k-\frac{1}{2}$.

At this point, the corrected water heights of the reconstructed point values are non-negative. However, they may be very small or even zero. Because $u = \frac{hu}{h}$ and $v = \frac{hv}{h}$, these computations may lead to large errors in the partially flooded cells for small water heights, and they have a singularity at zero water height ($h = 0$). To deal with this problem, we use the desingularization suggested in [23]:

$$u = \frac{\sqrt{2}h(hu)}{\sqrt{h^4 + \max(h^4, \epsilon)}}, \quad v = \frac{\sqrt{2}h(hv)}{\sqrt{h^4 + \max(h^4, \epsilon)}}, \tag{35}$$

where ϵ is a small a priori chosen positive number. This has a dampening effect on the velocities as the water height approaches zero. Determining a proper value for ϵ is very difficult. High values lead to large errors in the simulation results, while low values give small time steps. In our simulation, we used the suggestion of Brodtkorb [43]:

$$\epsilon = E_0 \max\left(1, \min\left(\Delta x, \Delta y\right)\right), \tag{36}$$

with $E_0 = 10^{-2}$.

5. POSITIVITY PRESERVING IN TIME INTEGRATION

In the previous section, we have discussed the well-balanced spatial reconstruction of the point values for partially flooded cells. In this section, we continue with the time-quadrature for the fluxes at partially flooded cells. This means the discretization of the semi-discrete scheme in time and advancing by Δt. We follow the technique used in [14] and start with modifying the time integration of the water height so that it remains positive after its computation. Assuming that the water height is positive for all $\bar{h}^n_{j,k}$ at time step n, it has to remain positive for the next time step $n+1$:

$$\bar{h}^{n+1}_{j,k} = \bar{h}^n_{j,k} - \Delta t \frac{(\mathbf{H}^x)^{(1)}_{j+\frac{1}{2},k} - (\mathbf{H}^x)^{(1)}_{j-\frac{1}{2},k}}{\Delta x} - \Delta t \frac{(\mathbf{H}^y)^{(1)}_{j,k+\frac{1}{2}} - (\mathbf{H}^y)^{(1)}_{j,k-\frac{1}{2}}}{\Delta y} \geqslant 0, \tag{37}$$

where we use Equation (22) and subtract $B_{j,k}$ from both sides because $\bar{w}_{j,k} = \bar{h}_{j,k} + B_{j,k}$.

Using Equation (37) we introduce the draining time step [27] for the two-dimensional scheme:

$$\Delta t^{drain}_{j,k} = \frac{\Delta x \Delta y \bar{h}^n_{j,k}}{\Delta y \left((\mathbf{H}^x)^{(1)}_{j+\frac{1}{2},k} + (\mathbf{H}^x)^{(1)}_{j+\frac{1}{2},k}\right) + \Delta x \left((\mathbf{H}^y)^{(1)}_{j,k+\frac{1}{2}} + (\mathbf{H}^y)^{(1)}_{j,k+\frac{1}{2}}\right)}, \tag{38}$$

which describes how long it takes for cell $C_{j,k}$ to become dry because of the outflow fluxes. Now, we modify the evolution step in Equation (22) using the draining time step:

$$\bar{h}^{n+1}_{j,k} = \bar{h}^n_{j,k} - \Delta t_{j,k} \frac{(\mathbf{H}^x)^{(1)}_{j+\frac{1}{2},k} - (\mathbf{H}^x)^{(1)}_{j-\frac{1}{2},k}}{\Delta x} - \Delta t_{j,k} \frac{(\mathbf{H}^y)^{(1)}_{j,k+\frac{1}{2}} - (\mathbf{H}^y)^{(1)}_{j,k-\frac{1}{2}}}{\Delta y}, \tag{39}$$

DOI: 10.1002/fld

where the time steps at the cell interfaces are computed by

$$\Delta t_{j,k} = \begin{cases} \min\left(\Delta t, \Delta t_{j,k}^{drain}\right), & \text{if } \nabla \cdot \mathbf{H}_{j,k} > 0, \\ \Delta t, & \text{if } \nabla \cdot \mathbf{H}_{j,k} \leqslant 0, \end{cases} \tag{40}$$

which means that the draining time step is only used if the water height decreases during the integration and the cell is at risk of drying out. If the flux divergence $\nabla \cdot \mathbf{H}_{j,k} > 0$ for a fully flooded cell $C_{j,k}$, then the draining time can have higher values than the global time step, and we select the smallest of the two. If $\nabla \cdot \mathbf{H}_{j,k} \leqslant 0$, that is, there is more water entering than leaving the cell, then we use the global time step. This means that the draining time step is applied only to the partially flooded cell in case of the positive divergence. Hence, the time evolution of the fully flooded cells remains as in [23].

Because we use the global time step Δt for the source terms $\bar{S}_{j,k}^{(2)}$ and $\bar{S}_{j,k}^{(3)}$ in the time evolution step, we have to split the momentum fluxes $F^{(2)}(\mathbf{U}, B)$ and $G^{(3)}(\mathbf{U}, B)$ into advection (a) and gravity-driven (g) parts to ensure the well-balanced property:

$$\begin{aligned} F^{(2),a}(\mathbf{U}, B) &:= \frac{(hu)^2}{w - B} \quad \text{and} \quad F^{(2),g}(\mathbf{U}, B) &:= \frac{\mathrm{g}}{2}(w - B)^2 \\ G^{(3),a}(\mathbf{U}, B) &:= \frac{(hv)^2}{w - B} \quad \text{and} \quad G^{(3),g}(\mathbf{U}, B) &:= \frac{\mathrm{g}}{2}(w - B)^2. \end{aligned}$$

Because of this modification, the source terms exactly balance the gravity-driven part of the flux. Using the split fluxes, the modified central-upwind fluxes read

$$\begin{aligned} \mathbf{H}_{j,k+\frac{1}{2}}^{(3),g}(t) = &\frac{a_{j,k+\frac{1}{2}}^{+}\mathbf{G}^{(3),g}\left(\mathbf{U}_{j,k+\frac{1}{2}}^{-}\right) - a_{j,k+\frac{1}{2}}^{-}\mathbf{G}^{(3),g}\left(\mathbf{U}_{j,k+\frac{1}{2}}^{+}\right)}{a_{j,k+\frac{1}{2}}^{+} - a_{j,k+\frac{1}{2}}^{-}} \\ &+ \frac{a_{j,k+\frac{1}{2}}^{+}a_{j,k+\frac{1}{2}}^{-}}{a_{j,k+\frac{1}{2}}^{+} - a_{j,k+\frac{1}{2}}^{-}}\left[\mathbf{U}_{j,k+\frac{1}{2}}^{(2),+} - \mathbf{U}_{j,k+\frac{1}{2}}^{(2),-}\right], \end{aligned} \tag{41}$$

and

$$\mathbf{H}_{j,k+\frac{1}{2}}^{(3),a}(t) = \frac{a_{j,k+\frac{1}{2}}^{+}\mathbf{G}^{(3),a}\left(\mathbf{U}_{j,k+\frac{1}{2}}^{-}\right) - a_{j,k+\frac{1}{2}}^{-}\mathbf{G}^{(3),a}\left(\mathbf{U}_{j,k+\frac{1}{2}}^{+}\right)}{a_{j,k+\frac{1}{2}}^{+} - a_{j,k+\frac{1}{2}}^{-}}. \tag{42}$$

The modified central-upwind fluxes $\mathbf{H}_{j+\frac{1}{2},k}^{(2),a}(t)$ and $\mathbf{H}_{j+\frac{1}{2},k}^{(2),g}(t)$ can be derived analogously, and their one-dimensional forms can be found in [14], which are very similar to the two-dimensional ones.

Using the new fluxes, we get the new update of discharges hu and hv:

$$\begin{aligned} \bar{hu}_{j,k}^{n+1} = \bar{hu}_{j,k}^{n} - \Delta t \bar{S}_{j,k}^{(2),n} - \Delta t \frac{(\mathbf{H}^x)_{j+\frac{1}{2},k}^{(2),g} - (\mathbf{H}^x)_{j-\frac{1}{2},k}^{(2),g}}{\Delta x} \\ - \Delta t_{j,k}\left(\frac{(\mathbf{H}^y)_{j,k+\frac{1}{2}}^{(2)} - (\mathbf{H}^y)_{j,k-\frac{1}{2}}^{(2)}}{\Delta y} - \frac{(\mathbf{H}^x)_{j+\frac{1}{2},k}^{(2),a} - (\mathbf{H}^x)_{j-\frac{1}{2},k}^{(2),a}}{\Delta x}\right) \end{aligned} \tag{43}$$

DOI: 10.1002/fld

$$\begin{aligned}\bar{hv}_{j,k}^{n+1} &= \bar{hv}_{j,k}^{n} - \Delta t\,\bar{S}_{j,k}^{(3),n} - \Delta t\,\frac{(\mathbf{H}^y)_{j,k+\frac{1}{2}}^{(3),g} - (\mathbf{H}^y)_{j,k-\frac{1}{2}}^{(3),g}}{\Delta y} \\ &\quad - \Delta t_{j,k}\left(\frac{(\mathbf{H}^x)_{j+\frac{1}{2},k}^{(3)} - (\mathbf{H}^x)_{j-\frac{1}{2},k}^{(3)}}{\Delta x} - \frac{(\mathbf{H}^y)_{j,k+\frac{1}{2}}^{(3),a} - (\mathbf{H}^y)_{j,k-\frac{1}{2}}^{(3),a}}{\Delta y}\right)\end{aligned} \tag{44}$$

This new finite volume scheme consisting of Equations (39), (43), and (44) is both well balanced and positivity preserving even in the presence of partially flooded cells.

As in [14] for the one-dimensional scheme, we prove that the new two-dimensional central-upwind finite volume scheme remains well balanced for both 'lake at rest' and 'dry lake' states.

Theorem 1
Consider the system in Equation (1) and the fully discrete central-upwind scheme in Equations (39), (43), and (44). Assume that the numerical solution $\mathbf{U}(t^n)$ corresponds to the steady state, which is a combination of the 'lake at rest' (Equation 3) and 'dry lake' (Equation 4) states in the sense that $w_{j,k} = \text{Const.}$, and $u = 0, v = 0$ whenever $h_{j,k} > 0$. Then $\mathbf{U}(t^{n+1}) = \mathbf{U}(t^n)$, that is, the scheme is well balanced.

Proof
We have to show that in all cells, the fluxes and the source term discretization cancel exactly. First, we mention the fact that the reconstruction procedure derived in Section 4 preserves both the 'lake at rest' and 'dry lake' steady states and their combinations. For all cells where the original reconstruction is not corrected, the resulting slopes are zero, and therefore, the reconstructed point values equal to the average water level there, $w_{j\pm\frac{1}{2}}^{\mp} = w_{j,k}$. As $hu = 0$ and $hv = 0$ in all cells, the reconstructions for hu and hv reproduce the constant point values $(hu)_{j\pm\frac{1}{2},k}^{\mp} = (hu)_{j,k\pm\frac{1}{2}}^{\mp} = (hv)_{j\pm\frac{1}{2},k}^{\mp} = (hv)_{j,k\pm\frac{1}{2}}^{\mp} = 0, \forall j,k$. Thus, the draining time is equal to the global time step, that is, $\Delta t_{j,k}^{drain} = \Delta t$.

First, we show that the update of the water levels satisfies the aforementioned criteria:

$$\begin{aligned}\mathbf{H}_{j+\frac{1}{2},k}^{(1),x} &= \frac{a_{j+\frac{1}{2},k}^{+}(hu)_{j+\frac{1}{2},k}^{-} - a_{j+\frac{1}{2},k}^{-}(hu)_{j+\frac{1}{2},k}^{+}}{a_{j+\frac{1}{2},k}^{+} - a_{j+\frac{1}{2},k}^{-}} \\ &\quad + \frac{a_{j+\frac{1}{2},k}^{+}a_{j+\frac{1}{2},k}^{-}}{a_{j+\frac{1}{2},k}^{+} - a_{j+\frac{1}{2},k}^{-}}\left[(h+B)_{j+\frac{1}{2},k}^{+} - (h+B)_{j+\frac{1}{2},k}^{-}\right] = 0,\end{aligned}$$

as $B_{j+\frac{1}{2},k}^{+} = B_{j+\frac{1}{2},k}^{-}$, $h_{j+\frac{1}{2},k}^{+} = h_{j+\frac{1}{2},k}^{-}$ and $(hu)_{j+\frac{1}{2}}^{+} = (hu)_{j+\frac{1}{2},k}^{-} = 0$. The same holds for $\mathbf{H}_{j,k+\frac{1}{2}}^{(1),y}$ with hv. From this, we get

$$\bar{w}_{j,k}^{n+1} = \bar{h}_{j,k}^{n+1} + B_{j,k} = \bar{h}_{j,k}^{n} + B_{j,k} = \bar{w}_{j,k}^{n}.$$

Second, we analyze the update of the discharge using Equations (43) and (44). Using the same argument and setting $u_{j+\frac{1}{2},k}^{\pm} = u_{j,k+\frac{1}{2}}^{\pm} = v_{j+\frac{1}{2},k}^{\pm} = v_{j,k+\frac{1}{2}}^{\pm} = 0$ at the points $p^x = p_{j+\frac{1}{2},k}$ and $p^y = p_{j,k+\frac{1}{2}}$, where $h_{j+\frac{1}{2},k}^{+} = h_{j+\frac{1}{2},k}^{-} = h_{j,k+\frac{1}{2}}^{+} = h_{j,k+\frac{1}{2}}^{-} = 0$ for the second and third component, we obtain

DOI: 10.1002/fld

$$
\begin{aligned}
\mathbf{H}^{(2),a,x}_{j+\frac{1}{2},k}+\mathbf{H}^{(2),g,x}_{j+\frac{1}{2},k} &= \frac{a^+_{j+\frac{1}{2},k}(hu)^-_{j+\frac{1}{2},k}-a^-_{j+\frac{1}{2},k}(hu)^+_{j+\frac{1}{2},k}}{a^+_{j+\frac{1}{2},k}-a^-_{j+\frac{1}{2},k}}\\
&\quad+\frac{a^+_{j+\frac{1}{2},k}\left(\frac{\mathrm{g}}{2}h^2\right)^-_{j+\frac{1}{2},k}-a^-_{j+\frac{1}{2},k}\left(\frac{\mathrm{g}}{2}h^2\right)^+_{j+\frac{1}{2},k}}{a^+_{j+\frac{1}{2},k}-a^-_{j+\frac{1}{2},k}}\\
&\quad+\frac{a^+_{j+\frac{1}{2},k}a^-_{j+\frac{1}{2},k}}{a^+_{j+\frac{1}{2},k}-a^-_{j+\frac{1}{2},k}}\left[(hu)^+_{j+\frac{1}{2},k}-(hu)^-_{j+\frac{1}{2},k}\right]\\
&=\frac{\left(u_{j+\frac{1}{2},k}+\sqrt{\mathrm{g}h_{j+\frac{1}{2},k}}\right)\left(\frac{\mathrm{g}}{2}h^2\right)^-_{j+\frac{1}{2},k}-\left(u_{j+\frac{1}{2},k}-\sqrt{\mathrm{g}h_{j+\frac{1}{2},k}}\right)\left(\frac{\mathrm{g}}{2}h^2\right)^+_{j+\frac{1}{2},k}}{\left(u_{j+\frac{1}{2},k}+\sqrt{\mathrm{g}h_{j+\frac{1}{2},k}}\right)-\left(u_{j+\frac{1}{2},k}-\sqrt{\mathrm{g}h_{j+\frac{1}{2},k}}\right)}\\
&=\frac{\mathrm{g}}{2}h^2_{j+\frac{1}{2},k}
\end{aligned}
\tag{45}
$$

$$
\begin{aligned}
\mathbf{H}^{(2),y}_{j+\frac{1}{2},k} &= \frac{a^+_{j+\frac{1}{2},k}(huv)^-_{j+\frac{1}{2},k}-a^-_{j+\frac{1}{2},k}(huv)^+_{j+\frac{1}{2},k}}{a^+_{j+\frac{1}{2},k}-a^-_{j+\frac{1}{2},k}}\\
&\quad+\frac{a^+_{j+\frac{1}{2},k}a^-_{j+\frac{1}{2},k}}{a^+_{j+\frac{1}{2},k}-a^-_{j+\frac{1}{2},k}}\left[(huv)^+_{j+\frac{1}{2},k}-(huv)^-_{j+\frac{1}{2},k}\right]=0,
\end{aligned}
\tag{46}
$$

where

$$
\begin{aligned}
h_{j+\frac{1}{2},k} &:= h^+_{j+\frac{1}{2},k}=h^-_{j+\frac{1}{2},k} \quad \text{and} \quad h_{j,k+\frac{1}{2}} := h^+_{j,k+\frac{1}{2}}=h^-_{j,k+\frac{1}{2}},\\
u_{j+\frac{1}{2},k} &:= u^+_{j+\frac{1}{2},k}=u^-_{j+\frac{1}{2},k} \quad \text{and} \quad u_{j,k+\frac{1}{2}} := u^+_{j,k+\frac{1}{2}}=u^-_{j,k+\frac{1}{2}}.
\end{aligned}
$$

Following the same rules, it can straightforwardly be proven that $\mathbf{H}^{(3),a,y}_{j,k+\frac{1}{2}}+\mathbf{H}^{(3),g,y}_{j,k+\frac{1}{2}}=\frac{\mathrm{g}}{2}h^2_{j,k+\frac{1}{2}}$ and $\mathbf{H}^{(3),x}_{j,k+\frac{1}{2}}=0$. Therefore, the finite update in Equations (43)– (44) for the studied steady state after substituting the source quadrature in Equations (9)–(10) reads as

$$
\begin{aligned}
(\bar{hu})^{n+1}_{j,k} &= (\bar{hu})^n_{j,k}-\frac{\Delta t}{\Delta x}\left[\frac{g}{2}\left(h_{j+\frac{1}{2},k}\right)^2-\frac{g}{2}\left(h_{j-\frac{1}{2},k}\right)^2\right]+\Delta t\,\bar{\mathbf{S}}^{(2),n}_{j,k}\\
&= (\bar{hu})^n_{j,k}-\frac{\Delta t}{\Delta x}\left[\frac{g}{2}\left(h_{j+\frac{1}{2},k}\right)^2-\frac{g}{2}\left(h_{j-\frac{1}{2},k}\right)^2\right]+\frac{\Delta t}{\Delta x}g\bar{h}_{j,k}\left(B_{j+\frac{1}{2},k}-B_{j+\frac{1}{2},k}\right)\\
&= (\bar{hu})^n_{j,k},
\end{aligned}
$$

where we have used

$$
\frac{\left(h_{j+\frac{1}{2},k}\right)^2-\left(h_{j-\frac{1}{2},k}\right)^2}{2}=-\bar{h}^n_{j,k}\left(B_{j+\frac{1}{2},k}-B_{j-\frac{1}{2},k}\right),
\tag{47}
$$

$$
\frac{\left(h_{j,k+\frac{1}{2}}\right)^2-\left(h_{j,k-\frac{1}{2}}\right)^2}{2}=-\bar{h}^n_{j,k}\left(B_{j,k+\frac{1}{2}}-B_{j,k-\frac{1}{2}}\right).
\tag{48}
$$

DOI: 10.1002/fld

We have to verify Equations (47) and (48). In the fully flooded cells, where $w_{j,k} > B_{j\pm\frac{1}{2},k}$, we have

$$\begin{aligned}\frac{\left(h_{j+\frac{1}{2},k}\right)^2-\left(h_{j-\frac{1}{2},k}\right)^2}{2} &= \frac{h_{j+\frac{1}{2},k}+h_{j-\frac{1}{2},k}}{2}\left(h_{j+\frac{1}{2},k}-h_{j-\frac{1}{2},k}\right)\\ &= \bar{h}^n_{j,k}\left(w_{j,k}-B_{j+\frac{1}{2},k}-w_{j,k}-B_{j-\frac{1}{2},k}\right)=-\bar{h}^n_{j,k}\left(B_{j+\frac{1}{2},k}-B_{j-\frac{1}{2},k}\right)\end{aligned} \tag{49}$$

and thus, Equation (47) is satisfied. One can easily prove the same for Equation (48). It remains to verify the solution for

$$\begin{aligned}(\bar{hv})^{n+1}_{j,k} &= (\bar{hv})^n_{j,k}-\frac{\Delta t}{\Delta y}\left[\frac{g}{2}\left(h_{j,k+\frac{1}{2}}\right)^2-\frac{g}{2}\left(h_{j,k-\frac{1}{2}}\right)^2\right]+\Delta t\,\bar{\mathbf{S}}^{(3),n}_{j,k}\\ &= (\bar{hv})^n_{j,k}-\frac{\Delta t}{\Delta y}\left[\frac{g}{2}\left(h_{j,k+\frac{1}{2}}\right)^2-\frac{g}{2}\left(h_{j,k-\frac{1}{2}}\right)^2\right]+\frac{\Delta t}{\Delta y}g\bar{h}_{j,k}\left(B_{j,k+\frac{1}{2}}-B_{j,k+\frac{1}{2}}\right)\\ &= (\bar{hv})^n_{j,k}\end{aligned}$$

which can be satisfied by using Equation (48). In the partially flooded cells, where $w_{j,k} < B_{j-\frac{1}{2},k}$, we have $h_{j-\frac{1}{2},k}=0$, and thus, using Equations (32) and (47) yields

$$\frac{\left(h_{j+\frac{1}{2},k}\right)^2}{2}=\frac{\Delta x^*_{j,k}h_{j+\frac{1}{2},k}}{2\Delta x}\left(B_{j+\frac{1}{2},k}-B_{j+\frac{1}{2},k}\right)=-\frac{h_{j+\frac{1}{2},k}}{2}\Delta x^*_{j,k}(B_x)_{j,k}, \tag{50}$$

which is true because at the studied steady situation, $x^*_{j,k}=x^*_w$, which implies that $\Delta x^*_{j,k}=\Delta x^*_w$, and hence, $-\Delta x^*_{j,k}(B_x)_{j,k}=h_{j+\frac{1}{2},k}$. Finally, we show the same for $w_{j,k} < B_{j,k-\frac{1}{2}}$, $h_{j,k-\frac{1}{2}}=0$ using Equation (48):

$$\frac{\left(h_{j,k+\frac{1}{2}}\right)^2}{2}=\frac{\Delta y^*_{j,k}h_{j,k+\frac{1}{2}}}{2\Delta y}\left(B_{j,k+\frac{1}{2}}-B_{j,k+\frac{1}{2}}\right)=-\frac{h_{j,k+\frac{1}{2}}}{2}\Delta y^*_{j,k}(B_y)_{j,k}, \tag{51}$$

which is also true because $y^*_{j,k}=y^*_w$. This implies that $\Delta y^*_{j,k}=\Delta y^*_w$, and hence, $-\Delta y^*_{j,k}(B_y)_{j,k}=h_{j,k+\frac{1}{2}}$.

This concludes the proof of the theorem. □

6. EVALUATION

The new scheme proposed in this paper is denoted as HWP14 scheme. In order to test the scheme and compare it with an existing scheme, we implemented the HWP14 and KP07 [23] schemes for computation on graphics processing units. We then performed a number of numerical experiments. As a first step, we analyzed a wave run-up on a slope. This simulation is followed by a verification against a two-dimensional parabolic basin benchmark for which an analytical solution exists. To demonstrate the stability and to measure the performance of the schemes, we created two real-world scenarios. The first is a breach-initiated flood in an urban area, and the second is a flood event in a rural area.

6.1. Wave run-up on a slope

In this comparison, we compare the schemes on a small domain, where we simulate a wave run-up on a slope. We let the water oscillate for 1000 seconds and visualize the results (Figure 8). For the

DOI: 10.1002/fld

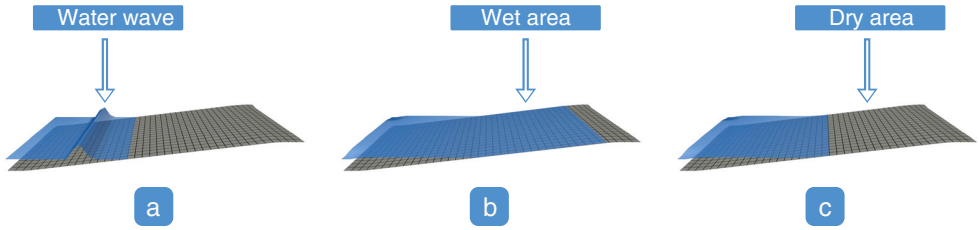

Figure 8. Comparison of drying of the KP07 and the HWP14 schemes. We simulate a wave run-up on a slope and visualize the solution after 1000 seconds. (a) Initial condition. (b) Solution of the KP07 scheme, where the upper part of the simulation domain is wet. There is a thin layer of water, which is incorrect. (c) Solution of the HWP14 scheme, the upper part of the domain is dry.

KP07 scheme, the upper part of the domain does not dry out. If a cell becomes wet, it will always contain a very thin layer of water and will never dry out again. For the HWP14 scheme, the upper part of the slope dries out because of the new reconstruction and draining time step technique.

6.2. *Parabolic basin benchmark*

The analytical solution of the parabolic basin case was first introduced by Thacker [44]. It describes time-dependent oscillations of planar water surface in a parabolic basin. It serves as a good basis to compare different numerical schemes [22, 45–48]. Recently, Sampson *et al.* [48] extended the solution of Thacker to support bed friction. However, their solution is limited to one dimension. In this two-dimensional case, we use the same setup as Holdahl *et al.* [49]. The bathymetry of the two-dimensional parabolic basin is given by

$$B(x, y) = D_0 \left(\frac{x^2 + y^2}{L^2} - 1 \right). \tag{52}$$

The water surface elevation and the velocities are given by

$$\begin{aligned} w(x, y) &= 2AD_0 \left(x \cos \omega t \pm y \sin \omega t + LB_0\right) \\ u(x, y) &= -A \cos \omega t \\ u(x, y) &= \pm A \sin \omega t \end{aligned} \qquad \omega = \sqrt{\frac{2D_0}{L^2}}, \tag{53}$$

where we set $D_0 = 1$, $L = 2500$, $A = \frac{L}{2}$, $B_0 = -\frac{A}{2L}$, the gravitational constant $g = 1$, the desingularization $\epsilon = 0.01$, and use 100×100 grid cells with a second-order accurate Runge–Kutta time integrator. Figure 9 shows our simulation results for two snapshots in time, where we compare the solutions of the numerical solvers to the analytical one. We visualize a one-dimensional slice in x-dimension in the middle of the computation domain. We plot values $w_{j,k}$ at cell centers, which are the average values. Both the KP07 and the HW14 schemes capture well the water levels of the analytical solution. However, there is an error accumulating for the velocities along the wet/dry boundaries. This can be found in many schemes [8, 23, 49], and it is difficult to avoid. We can reduce the error by setting the desingularization ϵ to a higher value. However, higher ϵ values cause spurious oscillations in the KP07 scheme, which were not observed in the HWP14 scheme. Furthermore, for small water heights, numerical errors can be introduced when calculating the velocity $u = hu/h$. This is related to a limited floating-point precision [50].

6.3. *Real-world performance benchmark in Cologne*

In the first real-world scenario, we simulate a levee breach in the city of Cologne, Germany. This scenario models a failure of the mobile flood protection walls, which are installed along the river to

DOI: 10.1002/fld

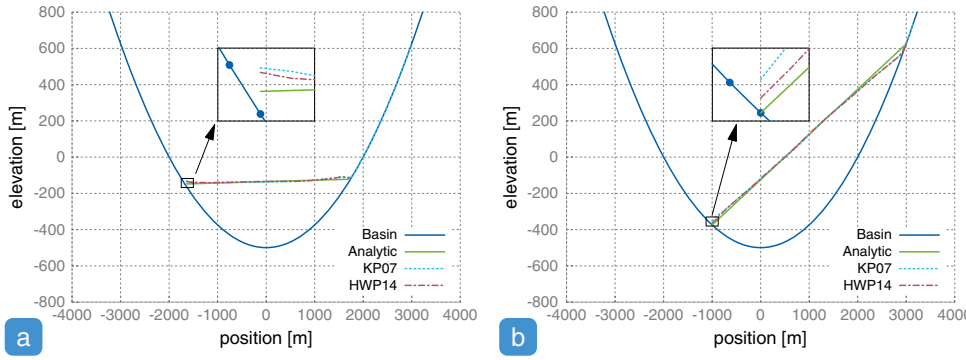

Figure 9. Simulation of oscillating water in a parabolic basin, compared with the analytical solution after (a) 300*s* and (b) 400*s*. Values are plotted at the cell centers. Blue dots in the inlay windows represent positions of the cell centers.

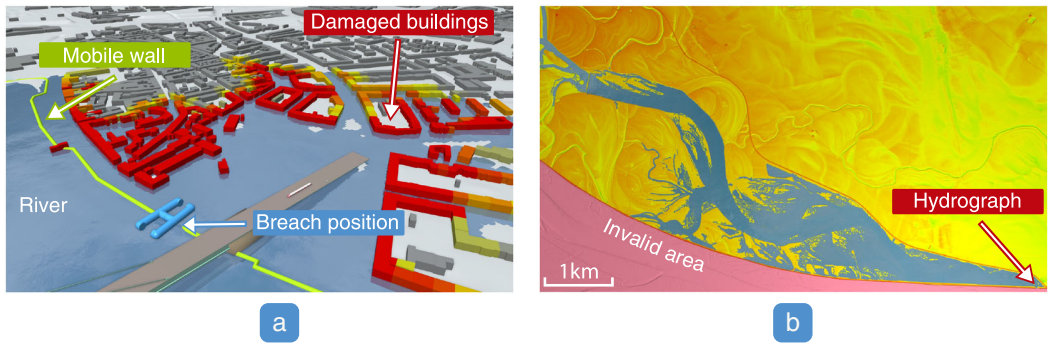

Figure 10. Real-world case studies. (a) Simulation of a levee breach caused by a failure of the mobile protection walls in the city of Cologne, Germany. The green line along the riverside represents the mobile protection wall. We removed a short section of the wall to simulate a breach (indicated in blue). The buildings are colored according to the damage, where red denotes high damage and grey no damage. (b) Results of a 5-day long hydrograph-based flood simulation in Lobau, Austria. The bathymetry is colored according to the elevation values. Red color represents higher altitudes, green color represents lower altitudes. Wet areas are shown in blue. The hydrograph is supplied for the short section at the bottom right corner.

protect the city. If the mobile wall collapses or the water height becomes high enough to overtop the walls, the city gets flooded. These two cases can happen in real-world situations, and it is important to understand their impacts.

In our case study, we simulate a 1 hour long levee breach. We simulate the breach by opening a short section of the mobile walls and letting the water flow into the city (Figure 10a). The buildings are colored based on the computed damage, where grey represents no damage, yellow is the middle damage, and red is the highest damage [51].

To assess the performance of our numerical scheme, we carried out a benchmark and compared the number of executed time steps (iterations) of the two schemes. A longer time step size requires fewer iterations to simulate the same duration and thus increases the performance. Figure 11 shows our performance results for a 60 minutes long simulation run. The size of the simulation domain is 1.4×1.6 kilometers, it contains 277×329 cells, where each cell is 5×5 meters large. In this case study, the KP07 scheme executes $\approx 4\times$ more time steps than the HWP14 scheme. The average time step per second is 0.08678 for the HWP14 scheme and 0.02253 for the KP07 scheme. The reason for this is that the KP07 scheme is not well balanced at the dry/wet boundaries; thus, high velocities appear at these locations. To keep the scheme stable, the CFL condition is applied. This means that the size of the actual time step is computed based on the highest velocity in the computation domain.

DOI: 10.1002/fld

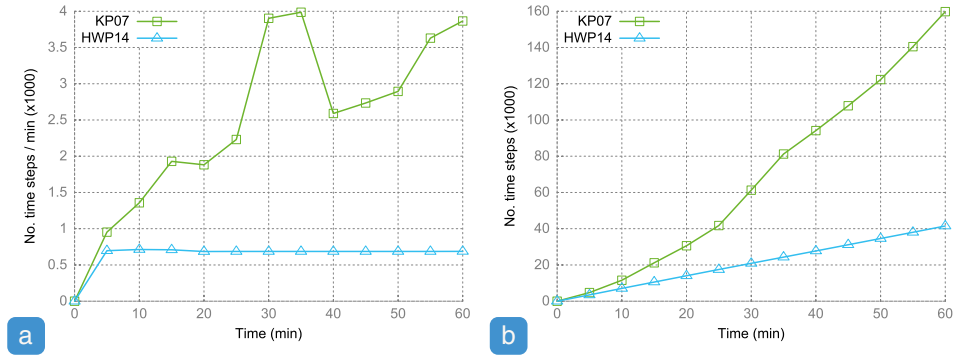

Figure 11. Real-world performance benchmark of a breach flood in the city of Cologne, Germany. We compare the time step performance of the KP07 and the HWP14 schemes. The figure shows the number of time steps as a function of the simulated time. Lower numbers corresponds to longer time step sizes in the simulation and thus to increased performance. (a) Average number of time steps per minute. (b) Cumulative number of time steps during the simulated 60 minutes.

Therefore, it acts as a limiting factor for the time step size. The HWP14 scheme does not suffer from this problem and can perform longer jumps in time while preserving numerical stability. We show both the instantaneous and cumulative number of time steps. Figure 11a shows the average number of time steps per minute. Figure 11b shows the total number of time steps for the 60 minutes long simulation run. During the first 5 minutes, the number of time steps is increasing as the water starts to flow into the city. After 5 minutes, as the flow starts to stabilize, the number of time steps in the HWP14 scheme is stabilizing too. In the KP07 scheme, the number of time steps continues to increase. Compared with the KP07 scheme, the HWP14 scheme is more stable with respect to the number of time steps.

6.4. Real-world performance benchmark in Lobau

The second case study involves the Lobau area, which is the alluvial backwater and floodplain of the Danube-Auen National Park. It extends on the left bank of the river Danube from river kilometer (rkm) 1918 to rkm 1908 downstream of the city of Vienna (Figure 10b). If the water level in the Danube rises, water flows from the river into the floodplain, causing regular flooding events. The size of the area is 1474 ha and it consists of floodplain forests and surface water bodies.

In this case study, we use a hydrograph from 13.01.2011 and simulate a 12 hours long flooding. The size of the simulation domain is 7.5×5 kilometers, it contains 2508×1682 cells, where each cell is 3×3 meters large. We simulate a period on 13.01.2011 for which we prescribe the hydrograph in the bottom right corner of the domain as a boundary condition. Both water level and discharge are prescribed. Discharge values describe the inflow from the Danube into the Lobau. Even though this is a rural area and does not contain any buildings, it is challenging to perform simulations for this region because it has a very complex bathymetry (lots of small channels and steep slopes). Here, we present only the first 12 hours of the simulation because the KP07 scheme slows down dramatically after 12 hours and 50 minutes. At this point, the actual time step size is $0.000156s$ and continues to decrease. The reason for this is that the velocities are accumulating and abnormally rising at the steep dry/wet boundaries limiting the time step size. Figure 12 shows the high-velocity spots, which are responsible for the simulation slow down. In the HWP14 scheme, the velocity profile is more consistent. For this special case, the HWP14 scheme was $\approx 8\times$ faster compared to the KP07 scheme during the 12 hours long simulation. This difference gets higher as the time advances. Using the HWP14 scheme, we have successfully performed a 168 hours long simulation, where the solver remained stable.

Our new HWP14 scheme executes approximately the same number of time steps in both case studies, which is below 1000 time steps per minute. The KP07 scheme is not as stable regarding

DOI: 10.1002/fld

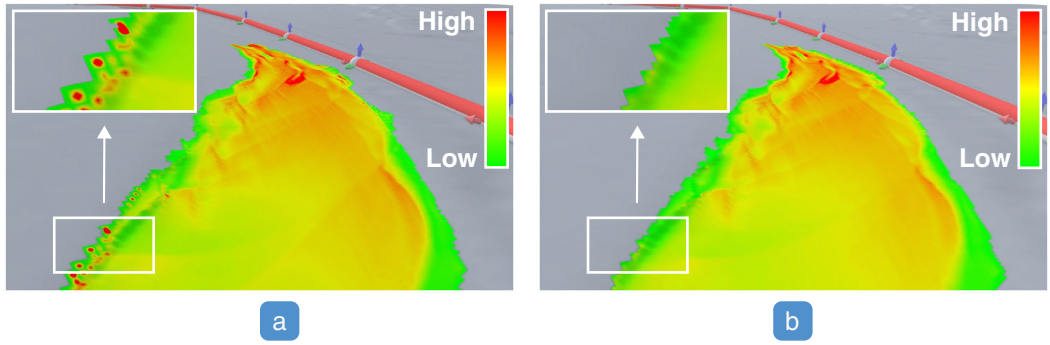

Figure 12. Velocity profile of the real-world simulation in Lobau. The bathymetry is colored according to the velocity magnitude. (a) Simulation results of the KP07 scheme. High-velocity spots (red) appear at the dry/wet boundaries. (b) Simulation results of the HWP14 scheme. No high-velocity spots, the velocity profile is consistent.

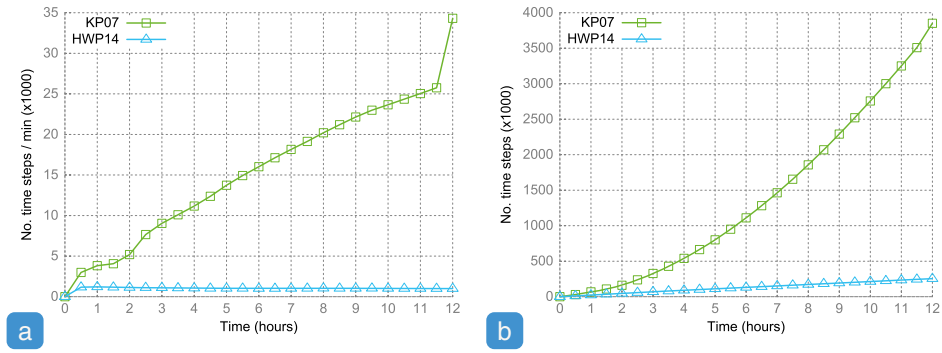

Figure 13. Real-world performance benchmark of a flood event in the Danube-Auen National Park, in Lobau, Austria. The figure shows the number of time steps as a function of the simulated time. Lower numbers correspond to longer time steps in the simulation and thus increased performance. (a) Average number of time steps per minute. (b) Total number of time steps during the simulated 12 hours.

the number of time steps. For the first case study, the average number of time steps is between 1000–4000 time steps per minute, while for the second case study, it is continuously increasing (Figure 13).

7. SUMMARY

We presented a two-dimensional numerical scheme for the Saint-Venant system of the SWE. We used a new two-dimensional reconstruction and a special correction procedure to ensure positive water heights and well-balanced states at partially flooded cells. The positivity of the water height is guaranteed by the draining time step, which is activated in the partially flooded cells if the divergence is positive. We proved that the scheme is well balanced and positivity preserving in the presence of partially flooded cells. Furthermore, it preserves 'lake at rest' and 'dry lake' steady states, as well as their combinations. The scheme was verified against the analytical solution of the parabolic basin benchmark. We measured and compared the time step performance of the KP07 and HWP14 schemes for two real-world scenarios. The first scenario was a flood event caused by a breach in the flood protection walls of the city of Cologne. The second scenario considered a flooding in the national park of Lobau near Vienna, where we used a hydrograph as a boundary condition to simulate the incoming flood from the Danube river. The new scheme proved its stability and it also proved to be faster than the KP07 scheme, as it needs fewer time steps to simulate the same time span because of the removal of spurious high velocities at the wet/dry boundaries.

DOI: 10.1002/fld

ACKNOWLEDGEMENTS

This work was supported by grants from the Austrian Science Fund project number W1219-N22 (Vienna Doctoral Programme on Water Resource Systems), from the Vienna Science and Technology Fund project number ICT12-009 (Scenario Pool), and from the European Research Council Advanced GrantİFlood-Change , project number 291152. We thank the flood protection centre of Steb Cologne, AöR, and the ViaDonau, Vienna, for supplying the terrain data.

REFERENCES

1. Brodtkorb AR, Sætra ML, Altinakar M. Efficient shallow water simulations on GPUs: Implementation, visualization, verification, and validation. *Computers & Fluids* 2010; **55**:1–12.
2. Acuña M, Aoki Takayuki. Real-time tsunami simulation on multi-node GPU cluster. *ACM/IEEE Conference on Supercomputing*, Portland, Oregon, 2009.
3. Di Baldassarre G, Montanari A, Lins H, Koutsoyiannis D, Brandimarte L, Blöschl G. Flood fatalities in Africa: From diagnosis to mitigation. *Geophysical Research Letters* 2010; **37**(22).
4. Hall J, Arheimer B, Borga M, Brázdil R, Claps P, Kiss A, Kjeldsen T R, KriaučinienŮ J, Kundzewicz Z W, Lang M, Llasat M C, Macdonald N, McIntyre N, Mediero L, Merz B, Merz R, Molnar P, Montanari A, Neuhold C, Parajka J, Perdigão R A P, Plavcová L, Rogger M, Salinas J L, Sauquet E, Schär C, Szolgay J, Viglione A, Blöschl G. Understanding flood regime changes in Europe: A state of the art assessment. *Hydrology and Earth System Sciences Discussions* 2013; **10**(12):15525–15624.
5. Perdigão RAP, Blöschl G. Spatio-temporal flood sensitivity to annual precipitation: Evidence for landscape-climate coevolution. *Water Resources Research* 2014; **50**(7):5492–5509.
6. Waser J, Konev A, Sadransky B, Horvth Z, Ribii H, Carnecky R, Kluding P, Schindler B. Many plans: Multidimensional ensembles for visual decision support in flood management. *Computer Graphics Forum* 2014; **33**(3): 281–290.
7. Hagen TR, Hjelmervik JM, Lie K-A, Natvig JR, Ofstad Henriksen M. Visual simulation of shallow-water waves. *Simulation Modelling Practice and Theory* 2005; **13**(8):716–726.
8. Kurganov Alexander, Levy Doron. Central-upwind schemes for the Saint-Venant system. *Mathematical Modelling and Numerical Analysis* 2002; **36**(3):397–425.
9. Temam Roger. Navier-Stokes equations. Theory and numerical analysis. 3rd (rev.) ed. *Studies in Mathematics and its Applications* 1984; **2**.
10. de la Asunción M, Mantas JM, Castro MJ. Programming CUDA-based GPUs to simulate two-layer shallow water flows. In *Euro-par 2010-parallel processing*. Springer: Springer Berlin Heidelberg, 2010.
11. Kurganov A, Petrova G. Central-upwind schemes for two-layer shallow water equations. *SIAM Journal on Scientific Computing* 2009; **31**(3):1742–1773.
12. Cunge JA, Wegner M. Intégration numérique des équations d'écoulement de barré de Saint-Venant par un schéma implicite de différences finies. *La Houille Blanche* 1964; **1**(1):33–39.
13. Zhou JG, Causon DM, Mingham CG, Ingram DM. The surface gradient method for the treatment of source terms in the shallow-water equations. *Journal of Computational Physics* 2001; **168**(1):1–25.
14. Bollermann A, Chen G, Kurganov A, Noelle S. A well-balanced reconstruction of wet/dry fronts for the shallow water equations. *Journal of Scientific Computing* August 2013; **56**(2):267–290.
15. Brandvik T, Pullan G. Acceleration of a two-dimensional Euler flow solver using commodity graphics hardware. *Proceedings of the Institution of Mechanical Engineers, Part C: Journal of Mechanical Engineering Science* 2007; **221**(12):1745–1748.
16. Brandvik T, Pullan G. Acceleration of a 3D Euler solver using commodity graphics hardware, 2008; 607.
17. De La Asunción M, Mantas J, Castro MJ. Simulation of one-layer shallow water systems on multicore and CUDA architectures. *The Journal of Supercomputing* 2011; **58**(2):206–214.
18. Lastra M, Mantas JM, Ureña C, Castro MJ, García-Rodríguez JA. Simulation of shallow-water systems using graphics processing units. *Mathematics and Computers in Simulation* 2009; **80**(3):598–618.
19. Noelle S, Pankratz N, Puppo G, Natvig JR. Well-balanced finite volume schemes of arbitrary order of accuracy for shallow water flows. *Journal of Computational Physics* 2006; **213**(2):474–499.
20. Russo G. Central schemes for conservation laws with application to shallow water equations. In *Trends and Applications of Mathematics to Mechanics*. Springer: Milan, 2005.
21. Xing Y, Shu C-W. High order finite difference WENO schemes with the exact conservation property for the shallow water equations. *Journal of Computational Physics* 2005; **208**(1):206–227.
22. Audusse E, Bouchut F, Bristeau M-O, Klein R, Perthame B. A fast and stable well-balanced scheme with hydrostatic reconstruction for shallow water flows. *SIAM Journal on Scientific Computing* 2004; **25**(6):2050–2065.
23. Kurganov A, Petrova G. A second-order well-balanced positivity preserving central-upwind scheme for the Saint-Venant system. *Communications in Mathematical Sciences* 2007; **5**(1):133–160.
24. Perthame B, Simeoni C. A kinetic scheme for the Saint-Venant system with a source term. *Calcolo* 2001; **38**(4): 201–231.
25. Courant R, Friedrichs K, Lewy Hans. On the partial difference equations of mathematical physics. *IBM journal of Research and Development* 1967; **11**(2):215–234.

DOI: 10.1002/fld

26. Gottlieb D, Tadmor E. The CFL condition for spectral approximations to hyperbolic initial-boundary value problems. *Mathematics of Computation* 1991; **56**(194):565–588.
27. Bollermann A, Noelle S, Lukácová-Medvidová M. Finite volume evolution Galerkin methods for the shallow water equations with dry beds. *Communications in Computational Physics* 2011; **10**:371–404.
28. Hinterberger C, Fröhlich J, Rodi W. Three-dimensional and depth-averaged large-eddy simulations of some shallow water flows. *Journal of Hydraulic Engineering* 2007; **133**(8):857–872.
29. Pankratz N, Natvig JR, Gjevik B, Noelle S. High-order well-balanced finite-volume schemes for barotropic flows: Development and numerical comparisons. *Ocean Modelling* 2007; **18**(1):53–79.
30. Tai Y-C, Noelle S, Gray JMNT, Hutter K. Shock-capturing and front-tracking methods for granular avalanches. *Journal of Computational Physics* 2002; **175**(1):269–301.
31. Bryson S, Epshteyn Y, Kurganov A, Petrova G. Well-balanced positivity preserving central-upwind scheme on triangular grids for the Saint-Venant system. *ESAIM: Mathematical Modelling and Numerical Analysis* 2011; **45**(3): 423–446.
32. Kurganov A, Noelle S, Petrova G. Semidiscrete central-upwind schemes for hyperbolic conservation laws and Hamilton–Jacobi equations. *SIAM Journal on Scientific Computing* 2001; **23**(3):707–740.
33. Lie K-A, Noelle S. On the artificial compression method for second-order nonoscillatory central difference schemes for systems of conservation laws. *SIAM Journal on Scientific Computing* 2003; **24**(4):1157–1174.
34. Nessyahu H, Tadmor E. Non-oscillatory central differencing for hyperbolic conservation laws. *Journal of Computational Physics* 1990; **87**(2):408–463.
35. Sweby PK. High resolution schemes using flux limiters for hyperbolic conservation laws. *SIAM Journal on Numerical Analysis* 1984; **21**(5):995–1011.
36. Van Leer B. Towards the ultimate conservative difference scheme. V. A second-order sequel to Godunov's method. *Journal of computational Physics* 1979; **32**(1):101–136.
37. Kröner D. *Numerical Schemes for Conservation Laws*, Vol. 22. Wiley Chichester, 1997.
38. LeVeque RJ. *Finite Volume Methods for Hyperbolic Problems*, Vol. 31. Cambridge university press, 2002.
39. Raviart P-A. *Numerical Approximation of Hyperbolic Systems of Conservation Laws*, Vol. 118. Springer, 1996.
40. Einfeldt B. On Godunov-type methods for gas dynamics. *SIAM Journal on Numerical Analysis* 1988; **25**(2):294–318.
41. Harten A, Lax PD, Leer B. On upstream differencing and Godunov-type schemes for hyperbolic conservation laws. *SIAM Review* 1983; **25**(1):35–61.
42. Bollermann A, Kurganov A, Noelle S. *A Well-balanced Reconstruction for Wetting, Drying Fronts*. Inst. für Geometrie und Praktische Mathematik: RWTH Aachen University, 2010.
43. Brodtkorb AR, Sætra ML, Altinakar M. Efficient shallow water simulations on GPUs: Implementation, visualization, verification, and validation. *Computers & Fluids* 2012; **55**:1–12.
44. Thacker WC. Some exact solutions to the nonlinear shallow-water wave equations. *Journal of Fluid Mechanics* 1981; **107**:499–508.
45. de la Asunción M, Castro MJ, Fernández-Nieto ED, Mantas JM, Acosta SO, González-Vida JM. Efficient GPU implementation of a two waves TVD-WAF method for the two-dimensional one layer shallow water system on structured meshes. *Computers & Fluids* 2013; **80**:441–452.
46. Gallardo JM, Parés C, Castro M. On a well-balanced high-order finite volume scheme for shallow water equations with topography and dry areas. *Journal of Computational Physics* 2007; **227**(1):574–601.
47. Liang Q, Marche F. Numerical resolution of well-balanced shallow water equations with complex source terms. *Advances in water resources* 2009; **32**(6):873–884.
48. Sampson J, Easton A, Singh M. Moving boundary shallow water flow above parabolic bottom topography. *Anziam Journal* 2006; **47**:C373–C387.
49. Holdahl R, Holden H, Lie K-A. Unconditionally stable splitting methods for the shallow water equations. *BIT Numerical Mathematics* 1999; **39**(3):451–472.
50. Whitehead N, Fit-Florea A. Precision & performance: Floating point and IEEE 754 compliance for NVIDIA GPUs. *rn (A+ B)* 2011; **21**:1–1874919424.
51. Ribicic H, Waser J, Fuchs R, Bloschl G, Groller Eduard. Visual analysis and steering of flooding simulations. *Visualization and Computer Graphics, IEEE Transactions on* 2013; **19**(6):1062–1075.

DOI: 10.1002/fld